SANDIA REPORT

Predicting Fracture in Micron-Scale Polycrystalline Silicon MEMS Structures

E. D. Reedy, Jr., B. L. Boyce, J. W. Foulk, III, R. V. Field, Jr., J. A. Ohlhausen,
M. P. de Boer, S. S. Hazra

Sandia National Laboratories

Predicting Fracture in Micron-Scale Polycrystalline Silicon MEMS Structures

E. D. Reedy, Jr.
R. V. Field, Jr.
Component Science & Mechanics

B. L. Boyce
Multiscale Metallurgical S&T

J. W. Foulk, III
Mechanics of Materials

J. A. Ohlhausen
Materials Characterization

Sandia National Laboratories
P.O. Box 5800
Albuquerque, NM 87185-0346

M. P. de Boer
S. S. Hazra
Carnegie Mellon University
Pittsburgh, PA 15213

Abstract

Designing reliable MEMS structures presents numerous challenges. Polycrystalline silicon fractures in a brittle manner with considerable variability in measured strength. Furthermore, it is not clear how to use a measured tensile strength distribution to predict the strength of a complex MEMS structure. To address such issues, two recently developed high throughput MEMS tensile test techniques have been used to measure strength distribution tails. The measured tensile strength distributions enable the definition of a threshold strength as well as an inferred maximum flaw size. The nature of strength-controlling flaws has been identified and sources of the observed variation in strength investigated. A double edge-notched specimen geometry was also tested to study the effect of a severe, micron-scale stress concentration on the measured strength distribution. Strength-based, Weibull-based, and fracture mechanics-based failure analyses were performed and compared with the experimental results.

Acknowledgements

Table of Contents

List of Figures

List of Tables

1. **Introduction**

Although micron-scale polycrystalline silicon (polySi) tensile bars can have average strengths of upwards of 3 GPa, they are extremely brittle. Like all brittle materials, the fracture strength is highly variable due to the inhomogeneity of critical flaws or defects. The strength of nominally identical polySi samples can vary by 50% [1]. Furthermore, the strength of a sample containing a micron-scale stress concentration depends on the size of the highly stressed region [2]. The material's brittleness suggests the use of a Weibull failure analysis. This type of failure analysis has often been applied with good success to brittle materials such as ceramics [3-4]. However, attempts to apply a Weibull failure analysis to micron-scale MEMS structures have shown such an approach to be inadequate [5-6]. An implicit assumption in a Weibull failure analysis is that a representative population of flaws is contained within a region that is small compared to specimen dimensions and stress gradients. This assumption is almost certainly not true for micron-scale stress concentrations in polySi MEMS structures. For example, samples fabricated using Sandia's SUMMiT V^{TM} microfabrication process can have side-wall flaws that are up to 90-nm deep [1] while the stress generated by a one micron stress concentrating feature would be expected to vary significantly over a distance that is 10% of the feature size.

Micron-scale tests that accurately measure the polySi strength distribution can provide crucial information defining brittle failure in MEMS structures. The lower tail of the strength distribution is of particular interest since this lower tail represents worst case failures. Such statistical data provides key information that can be used in developing a design methodology to avoid structural failure. Unfortunately, there is limited information on strength distribution tails as difficulties in testing micron-scale structures have limited testing to 10's of nominally identical tensile bars [1-2, 5-10]. Fortunately, the recent development of high throughput testing techniques has now enabled the testing of many 100's or even 1000's of nominally identical, micron-scale polySi tensile bars. In this paper we will report test results that define for the first time the character of the lower tail of the tensile strength distribution. These results, coupled with an examination of the factors that can generate variations in the measured strength, are used to develop a predictive, fracture mechanics-based failure analysis.

2. Experimental method

Two high throughput methods have been recently developed to test micron-scale, polySi tensile bars. The "on-chip" method developed by Hazra, et al. [11], uses an on-chip chevron thermal actuator to apply stress to an integral tensile specimen via a prehensile grip mechanism (Fig. 1). A free-standing tensile bar is connected to the substrate at one end and to a free-standing block with the female end of a prehensile grip mechanism at the other end. A thermal actuator that is attached to a shuttle that contains the male end of the grip mechanism is initially offset from the female end of the grip mechanism. During the insertion stage, an increasing potential difference applied across the legs of the thermal actuator generates an axial motion that pushes the male grippers forward. With

sufficient displacement, the male and female portions of the grip become fully latched and thus connect the tensile specimen to the thermal actuator. Upon cooling the thermal actuator by reducing the voltage, a monotonic normal tensile stress is applied as the thermal actuator pulls the specimen back until the specimen fractures. The tensile bar's end displacement is optically monitored at a gage located at the base of the tensile bar to ~2 nm resolution using pattern-matching and Moiré interferometric algorithms. The tensile specimens tested using the on-chip method were 2-µm wide and had a 70-µm gage length. Breaking stress is calculated from the measured end displacement by using a linear elastic finite element specimen calibration in conjunction with the nominal polySi modulus. See Ref. [11] for further details.

The "slack-chain" approach developed by Boyce [12], uses a custom built probe station to apply an external load to a chain of specimens (Fig. 2). This approach represents an extension to the earlier "pull-tab" method [1]. Here a chain of either 12 or 25 tensile specimens are tested sequentially without having to reposition the probe tip. The chain is designed so that each specimen fails independently; once a specimen fails additional displacement is required to take up slack in the chain of specimens before applying load to the next specimen. Load is measured during the test and stress is calculated using cross-sectional area. The tensile specimens tested using the slack-chain method had a nominal 2-µm width (actual as-fabricated width deviated somewhat from this value as discussed in detail later) and a 20-µm gage length. See Ref. [12] for further details. Most of the fracture data discussed in this paper was measured using the slack-chain method.

3. Tensile test data

All specimens tested in this study were fabricated using Sandia's SUMMiT V™ polySi microfabrication process [13]. The SUMMiT V™ process consists of four freestanding polySi layers. The present study is focused primarily on tensile bars fabricated from the third freestanding structural layer ("Poly3"), although for sake of comparison one set of tests were run on tensile bars from the fourth freestanding layer (Poly4). All samples were released in HF acid and rendered free-standing by critical point drying. Subsequently, most samples were coated by a molecular monolayer in a vapor-phase process (VSAM coating). The tested samples were fabricated in two different fabrication runs, and will be referred to by the reticule set with which they were processed, RS733 and RS784.

3.1 Slack-chain RS733 and RS784 Poly3 tensile tests

The slack-chain test method was used to test 616 tensile bars from RS733 and 671 tensile bars from RS784. The line width used in the calculation of tensile strength from the measured breaking force was based on the average line width of ~70 specimens from the same reticle set, where dimensions were determined from scanning electron microscope (SEM) images. RS733 had an average line width of 1.74 µm, while RS784 had an average line width of 1.88 µm. Both had a thickness of 2.33 µm based on parametric monitoring data. All of the RS733 samples and roughly half of the RS784 samples had a VSAM surface coating. Strength is treated as a random variable and Fig. 3 plots the

empirical cumulative distribution function (CDF) of the strength of RS733 and RS784 tensile bars. The plotted empirical CDFs for these two large datasets sets appear to be quite similar, and indeed a two-sample Kolmogorov-Smirnov test [14] indicates that the null hypothesis that measured RS733 and RS784 tensile strengths are from the same population cannot be rejected at the 5% significance level. This shows that the measured strength distribution is quite similar for two different processing runs and also suggests consistency in the slack-chain test method. Because of the statistical homogeneity of the RS733 and RS784 tensile test distributions, it is reasonable to create a composite, 1287 tensile strength data set (RS733-RS784). The measured tensile strengths ranged from 2.0 to 3.2 GPa.

The empirical CDF of the RS733-RS784 tensile strength data set is plotted, along with two and three parameter Weibull distribution fits, in Figs. 4 and 5, respectively. Note that the x- and y-axes have been scaled so that the Weibull CDF appears as a straight line. The 3-parameter Weibull strength distribution is defined by the expression

$$P = 1 - \exp\left[-\left(\frac{\sigma - \sigma_u}{\sigma_\theta} \right)^m \right]$$

(1)

where P x 100 is the percent of failed tensile samples, σ is measured strength, m is the Weibull modulus, $\sigma_\theta + \sigma_u$ is the characteristic strength, and σ_u is the threshold strength. The 2-parameter Weibull distribution is a special case of Eq. (1) obtained by setting $\sigma_u = 0$. A 3-parameter Weibull fit of RS733-RS784 is preferred to a 2-parameter fit based on p-value goodness-of-fit metrics (2-parameter: $p<0.010$; 3-parameter fit: $p=0.089$). A comparison of Figs. 4 and 5 clearly shows that the 3-parameter Weibull distribution fits the lower tail of the data better than a 2-parameter Weibull distribution. The measured RS733-RS784 tensile strength data set is consistent with the 95% confidence intervals for the 3-parameter fit (Fig. 5), while it falls well outside the 95% confidence interval on the 2-parameter Weibull fit (Fig. 4). Minitab 15 was used to perform the statistical analysis using a maximum likelihood estimate for fit parameters.

Table 1 lists the values of the 3-parameter Weibull fit parameters m, σ_θ, and σ_u along with their 95% confidence intervals (CI). Also shown are parameter values for individual fits of RS733 and RS784 so these can be contrasted with the composite fit of RS733-784. As expected, the parameters for all three fits are in reasonable agreement. Finally, note that the existence of a strength threshold is consistent with a another recently published, 1000-specimen tensile strength data set (RS686) [12]. This data was measured using an earlier version of the slack-chain design; the data presented in the current study uses a slightly modified version that improves reproducibility and minimizes systematic errors such as induced by frictional effects. The measured mean strengths of the three reticle sets RS686, RS733, and RS784 are quite similar: 2.56, 2.70, and 2.70 GPa, respectively. The threshold strength and Weibull modulii were also comparable within the 95% confidence bound (Table 1).

It has been previously reported that the tensile strength of the Poly4 layer is significantly higher than that of the Poly3 layer [1]. This has been confirmed by the present study. A

set of 591 Poly4 tensile bars from RS733 were tested (RS733-P4). These specimens were 2.35 μm thick, and had an average line width of 1.41 μm (based on parametric monitoring data and on ~70 SEM images, respectively). Figure 6 compares the empirical CDF of the strength of Poly4 tensile bars with that of RS733-RS784 Poly3 tensile bars. The mean tensile strength of RS733-P4 was 3.72 GPa; 38% then the mean tensile strength of RS733-RS784 Poly3 tensile bars. Weibull fit parameters for RS733 Poly4 strength data are listed in Table 1.

3.2 On-Chip RS784 Poly3 tensile tests

The on-chip test method was used to measure the strength of 231 tensile bars from RS784 (referred to as RS784-OC). Figure 7 plots the empirical CDF of the measured strengths. The measured tensile strengths ranged from 2.2 to 3.0 GPa with a mean strength of 2.5 GPa. As was the case for the slack-chain tensile data, a 3-parameter Weibull fit of RS784-OC is preferred to a 2-parameter fit based on *p*-value goodness-of-fit metrics (2-parameter: $p<0.010$; 3-parameter fit: $p=0.122$).This tensile data set is plotted, along with 2- and 3-parameter Weibull distribution fits, in Figs. 8 and 9, respectively. The measured RS784-OC tensile strength data set is clearly more consistent with the 3-parameter Weibull fit. Table 1 lists the values of the 3-parameter Weibull fit parameters along with their 95% confidence intervals. Note that the on-chip method is in a relatively early stage of its development. Although test results for only a couple of hundred tensile specimens are reported here, 1000-specimen tensile strength data sets could be measured if an automated probe station were used.

3.3 Flaw type and depth

To quantify the location and nature of the critical defects that cause fracture in SUMMiT V^{TM} polySi, SEM images of the fracture surface were collected for several hundred broken tensile bars. In many cases, hackle lines could be seen emanating away from the apparent crack origin, and in some cases a flat mirror-like facet could be identified at the apparent crack origin. These features allowed determination of the failure location of over 200 tensile bars. The fratogrpahic analysis, summarized in Appendix A, indicated that fracture initiated only along the sidewalls, with a clear preference for origins at bottom corners (the corners nearest to the substrate). No failures initiated in the middle of the top or bottom surfaces, nor did any failures initiate within the interior of the specimen. Consequently, strength-controlling flaws were limited to the sidewall. This observation is consistent with previously published tensile strength results of Chasiotis and Knauss [2]. They tested four specimen geometries fabricated using the SUMMiT V^{TM} process, two with a common width and two with a common length. They found that tensile strength scaled with specimen length rather than specimen width. This suggests that strength-controlling flaws are associated with the sidewall area, and not with total surface area or specimen volume. The location of the controlling defect is certainly dependent on the fabrication process: for example the MUMPs polySi process is typically associated with critical flaws on the top surface of the sample rather than the sidewalls [2].

AFM imaging was used to investigate the nature of pre-existing sidewall flaws. The AFM measurements were made with a Dimension Icon from Veeco Instruments using the instrument's "Peak Force Tapping" mode (Nanoscope 8.10 software), which controls the applied tip force to minimize tip wear and provide calibrated topographical information. To resolve sharp features line scans were taken with ~1.5 nm data point increments using Veeco's ScanAsyst Air AFM tips with a nominal 3-4 nm radius. Surface depth is defined relative to a mean reference surface (a 2nd-order plane with knots every 2.5 μm determined via a least squares fit of the raw AFM data). Local surface depth and curvature was determined by fitting a 6th order spline to each scan line with knots placed every 5 nm (~3 points). A local minimum in depth x_{min} corresponds to the tip of a flaw. Given the spline representation $f(x)$, the radius of curvature ρ_{min} at x_{min} is given by

$$\rho(x_{min}) = \frac{\left(1 + f'(x_{min})^2\right)^{\frac{3}{2}}}{f''(x_{min})} \qquad (2)$$

while the curvature $\kappa_{min} = 1/\rho_{min}$. This fitting procedure enables the description of every flaw in the AFM image in terms of its depth and root radius (i.e., radius of curvature).

Figure 10 shows a representative plot of Poly3 sidewall surface depth as determined from a fit of the raw AFM data. A 2.5 μm by 5.0 μm portion of the sidewall was scanned ($Y = 0$ corresponds to the edge of the scan that is closest to the bottom of the Poly3 layer). Micron-wide low spots appear as vertical bands (sidewall curtains) and contained within these regions are narrow grain boundary grooves that can be up to 45 nm deep. These grain boundary grooves are roughly V-shaped and are most likely generated by preferential etching of sidewall grain boundaries. Figure 11 plots curvature κ at points where there is a local minimum in the depth (i.e., tip of a flaw) for the same Poly3 sidewall as shown in Fig. 10. Figures 10 and 11 show that surface minima of substantial depth $d > 15$ nm and curvature $\kappa > 0.075$ 1/nm lie along the grain boundaries. Root radii that are as small as that which can be measured with a 3-4 nm radius AFM tip were found at some locations. Some grain boundary grooves appear to be almost crack-like since they can be both relatively deep and sharp.

AFM images permit a broad assessment of the type of sidewall flaws present. Unfortunately, the entire sidewall of each specimen cannot be scanned prior to testing. Consequently, the relatively rare but strength-controlling sidewall flaws in a tensile bar cannot be identified using this method. The complex topography of the grain boundary and associated edge flaws do suggest that different specimens will have different flaw populations and that there will be a range of strength-controlling flaw depths. The present methodology does provide detailed information on flaw depth and root radius that goes well beyond typical roughness metrics (average, root mean squared, skewness, etc.). Indeed this information enables a fracture analysis that is applied to actual AFM-images (Section 5).

3.4 Comparison of results from On-Chip and Slack-Chain methods

One cannot directly compare the tensile strength distributions measured by slack-chain and on-chip methods because the gage length L of the specimen used in each method differed. The slack-chain's specimen gage length is 20 μm, while the on-chip's specimen gage length is 70 μm. Within the 2-parameter Weibull framework (which does not fit the lower tail as well as the 3-parameter fit, but can be considered a rough approximation), the strength of a uniformly stressed tensile bar varies with sidewall area $A = 2Lh$ (h is specimen thickness) as

$$\frac{\sigma_2}{\sigma_1} = \left(\frac{A_1}{A_2}\right)^{1/m} \tag{3}$$

where σ_i is the tensile strength for a specimen with sidewall area A_i, m is the 2-parameter Weibull modulus, and where both strength values are for the same percent of failures [4]. The 2-parameter Weibull fit of the RS784 tensile data set yields $m = 16.8$, while a fit of the RS784-OC tensile data set yields $m=16.1$. Using an average m value of 16.5, Figure 12 shows that scaling RS784's empirical CDF ($L=20$ μm) by the factor $(20/70)^{1/16.5}=0.93$ (to estimate its empirical CDF for $L=70$ μm) brings it into good agreement with RS784-OC CDF ($L=70$ μm).

Beyond consistency in strengths, both test methods also indicate that there exists a threshold strength below which failure does not occur. This is true even though two very different test methods were employed (slack-chain and on-chip) and even though the tested specimens were processed during three different SUMMiT V™ fabrication runs (RS733 and RS784, along with previously published data on RS686 [12]). This is an important finding since it implies that there is a maximum controlling flaw size associated with the SUMMiT V™ fabrication process.

4. Other Potential Sources of Variability in Tensile Strength

The fractography analysis clearly shows that tensile failure in polySi is associated with sidewall flaws. Consequently, it is quite likely that the measured variation in tensile strength is closely linked to differences in the depth (or root radius, etc.) of sidewall flaws found in different samples. Indeed, differences in the strength-controlling flaws is thought to be the dominate source of tensile strength variability. There are, however, several other potential contributors to the variability in tensile strength, and these will be considered next. These include variations in line width, stress inhomogeneity within a polycrystal, and variations in the apparent fracture toughness. Note that the test methods used in this study do not appear to be a significant contributor to the measured variation in SUMMiT V™ tensile strength; these two very different test methods, which use quite different metrologies, generated similar empirical tensile strength CDFs (Fig. 12).

4.1 Line width

Variations within the SUMMiT V^{TM} polySi microfabrication process can generate modest variations in as-fabricated dimensions from the nominal design dimensions. We have observed that line width varies within an individual chip, between chips on a wafer, and between fabrication runs. To quantify such variations, the width of 77 tensile bars from RS733 and 73 tensile bars from RS784 were measured, with 3-4 width measurements per bar. The measured RS733 bars had an average width of 1.74 μm (0.04-μm standard deviation) with a minimum width of 1.66 μm and a maximum width of 1.82 μm. The measured RS784 bars had an average width of 1.88 μm (0.02-μm standard deviation) with a minimum width of 1.83 μm and a maximum width of 1.91 μm. This demonstrates that average line width can vary by ~ 10% within a fabrication run, as well as vary by ~10% between fabrication runs. These variations can have a direct impact on the measured tensile strength in those cases where force is measured and strength is calculated, as is done in the slack-chain test method (the on-chip method does not use line-width in the calculation of strength). In the present study, we used the average bar width measured for each individual fabrication run (e.g., RS733) to reduce some of the variability introduced in comparing different fabrication runs. It appears that line-width variations can contribute at most a modest portion of the measured variation in tensile strength. A more detailed description of line width observations and associated analysis is given in Appendix B.

4.2 Stress inhomogeneity within a polycrystal

It is well known that stress within a polycrystalline microstructure is not uniform. The crystallographic elastic anisotropy generates microstructural stress inhomogeneity and the stress inhomogeneity depends on crystal geometry, elastic properties, and crystal orientations. Indeed, within the context of linear elasticity, geometric and material discontinuities in a microstructure can generate a weak, crack-like, power-law singularity (i.e., weak compared to a crack or sharp V-notch) [15-16]. Accordingly, microstructurally induced stress variations could generate some of the measured variability in tensile strength. To investigate this possibility, illustrative calculations that explicitly model the columnar polycrystalline silicon microstructures were performed. To simplify the analysis and enable 2D, plane strain calculations, one axis of the crystal's cubic symmetry is taken to be aligned with the long axis of the columnar grain structure. Commonly accepted values of silicon crystal stiffness were used in all calculations (C_{11}=166 GPa, C_{12}=64 GPa, C_{66}=80 GPa). Silicon has a relatively weak cubic anisotropy. The level of crystal anisotropy is often characterized by the parameters R, where $R=(C_{12} + 2C_{66})/C_{11}$. R=1 for an isotropic material, R=1.35 for Si, and R=1.63 for Ni and Cu.

For polycrystalline aggregates composed of a relatively small number of grains, there will be variability in the average properties such as Young's modulus. To investigate this effect, finite element calculations were performed on model microstructures created using Voronoi tessellations. Square domains with n x n grains on a side (n=4, 6, 8, 12, and 16) were analyzed for the case of a tensile loading generated by a uniform edge displacement.

For each value of n, 25 different sets of random crystal rotations about the grains long axis were considered (drawn from a uniform distribution). This was done for four different tessellations. The calculated variation in Young's modulus E declined with n, but even when $n = 4$, the ratio of the standard deviation in E to the average value of E was only 0.025. Since the tensile bars are relatively long compared to the grain size (ratio estimated to be >50 for a silicon grain width of 0.4 μm), there should be little variability in the average tensile modulus between tensile specimens.

Random variations in the orientation of the crystals that bound an edge flaw could possibly generate variations in notch-tip stress fields and consequently generate variability in measured strength. The possibility that edge notches with the same geometry might have notch-tip stress fields that depend in a significant way on crystal orientation was investigated. Specifically, the Stroh formalism for anisotropic elasticity [17] was used to determine the asymptotic, singular stress state at the tip of a sharp V-notch between two silicon crystals with differing crystal orientations (Fig. 13). Note that the V-notch is assumed to be perpendicular to the edge and the grain boundary is aligned with the notch bisector. The use of the Stroh formalism to derive the characteristic equation governing the strength of the singularity at material and geometric discontinuities in anisotropic elastic materials is now well established and will not be discussed; only results will be presented here. The asymptotic solution for the V-notch problem has two singular terms.

$$\sigma_{ij} = \sum_{n=1}^{2} K_{an} r^{\lambda_n} f_{ijn}(\theta) \quad (i,j = r,\theta) \tag{4}$$

where r and θ refer to a polar coordinate system defined at the tip of the V-notch, K_{an} is a generalized stress intensity factors, λ_n is the strength of the singularity, and the function f_{ijn} defines the angular variation of the asymptotic stress field. For a V-notch between two silicon crystals, with a 60° wedge angle ($\omega_1 = -\omega_2 = 5\pi/6$, Fig. 13), the Stroh analysis indicates that λ_1 varies between -0.486 ($\gamma_a = 30^o$ and $\gamma_b = 60^o$) and -0.489 ($\gamma_a = 75^o$ and $\gamma_b = 15^o$), while λ_2 varies between -0.224 ($\gamma_a = 30^o$ and $\gamma_b = 60^o$) and -0.307 ($\gamma_a = 75^o$ and $\gamma_b = 15^o$). These values are quite close to the corresponding 60° V-notch results for a homogeneous, isotropic material where $\lambda_1 = -0.488$ and $\lambda_2 = -0.269$ [18]. Indeed, the strength of the strongest singularity, λ_1, shows little dependence on crystal orientation and its value is quite close to that of a sharp crack, -0.5.

Finally, the idealized problem of an edge V-notch in a tensile bar was analyzed (Fig. 14). A limited number of illustrative finite element calculations were performed to investigate the nature of the asymptotic, cleavage (i.e., hoop) stress generated in front of the notch. In these calculations a tensile bar with a 50-nm deep, 60° V-notch was subjected to a nominal 1% strain (1.6 GPa, nominal stress). The two crystals bounding the notch were modeled explicitly. These crystals each have a characteristic length $h = 200$ nm, and with crystal orientations defined by γ_a and γ_b (Fig. 14). The crystals were embedded within an effective isotropic material with properties chosen to be representative of a random aggregate of columnar silicon crystals where one axis of the crystal's cubic symmetry is taken to be aligned with the long axis of the columnar grain structure (E=156 GPa, $\nu = 0.22$, see Appendix C). For example, when $\gamma_a = 45^o$ and $\gamma_b = 0^o$, a power law fit of the

calculated cleavage stress σ_{22} shows it to be asymptotically singular with $\sigma_{22}=9359r^{-0.486}$, (Stroh analysis gives $\lambda=-0.488$) where r is distance from the notch tip. Likewise, when $\gamma_a=45^\circ$ and $\gamma_b=60^\circ$, the fit of the cleavage stress gives $\sigma_{22}=9763r^{-0.485}$ (Stroh analysis gives $\lambda=-0.487$). These results can be contrasted with those for the case where the tensile bar is fully homogeneous and isotropic and the V-notch is replaced by a sharp crack of the same depth, which results in $\sigma_{22}=9206r^{-0.500}$.

In summary, illustrative tensile bar calculations, along with the asymptotic results for the strength of the notch-tip singularity, suggest that the presence and orientation of silicon crystals at the notch tip have only a modest effect on the cleavage stress in front of a sharp V-notch. This conclusion is consistent with published results for the case of a long crack in a columnar polycrystalline silicon where many crystals are within the zone dominated by the crack-tip singularity [19]. Furthermore, a sharp edge crack in a homogeneous and isotropic material provides a reasonable approximation to an edge V-notch bounded by silicon crystals when the wedge opening angle is less than 60°. It does not appear that variations in notch-tip stress fields with crystal orientation contribute to measured variations in tensile strength.

4.3 Fracture toughness

Typical strength-controlling flaws are thought to lie along the grain boundary between two significantly larger crystals, where the crystal orientation can be random with respect to the grain boundary (see Fig. 14 for an idealized representation). AFM images of Poly3 sidewalls indicate that edge flaws are V-shaped with a depth of < 100 nm, while the width of a typical SUMMiT V^{TM} polySi columnar grain is ~400 nm. The K-like asymptotic stress field at the tip of a sharp V-notch edge flaw, which has a characteristic length that is only a fraction of the flaw depth, will dominate only a portion of the bounding grains. Furthermore, simple fracture mechanics arguments suggest that size of silicon's room temperature fracture process zone is quite small with an estimated size of approximately 2 nm [20]. Consequently, rapid crack growth is expected to occur while the crack still lies within the single crystal in which it initiated. Even if the crack were to grow stably to a length equal to the initial flaw depth, the crack would still lie within the crystal. On the other hand, the associated crack-tip stress intensity factor K would increase substantially. As a rough estimate, if the effective crack length doubled, K would increase by ~40% (follows from $K\sim\sigma a^{1/2}$, where a is crack length and σ is the fixed applied stress). Long crack toughening mechanisms, such as interactions with grain boundaries and growth into neighboring grains with different orientations, are not expected to be relevant [20]. Instead, local cleavage anisotropy is thought to dominate.

Silicon's reported cleavage anisotropy is rather modest and falls in the range of K_{IC} =0.83-0.95 MPa-m$^{1/2}$ with a standard deviation of about 0.1 MPa-m$^{1/2}$ in the measured data [20-22]. The variability in apparent toughness could be further enhanced by the fact that the cleavage plane is not necessarily aligned with the plane of peak cleavage stress. This, however, appears to be a minor effect; there is only a 6% decrease in the cleavage (hoop) stress in a 45° sector in front of a V-notch. Even if the cleavage plane is not aligned with the plane of maximum cleavage stress, only a modest increase in applied load should be needed to initiate crack growth. It appears that variations in the apparent

fracture toughness contributes to the variability in measured tensile strength, but it is not the dominate source of strength variability.

5. Fracture analysis of sidewalls as imaged by AFM

As discussed in Section 3.3, a new methodology for fitting raw AFM data was developed so that every flaw in an AFM image could be defined in terms of its depth and root radius (Figs. 10-11). This information can then be used in conjunction with a failure analysis to obtain a fundamental understanding of the origins of variability in the tensile strength. A coupled AFM/finite element analysis (AFM/FEA) of this type is summarized below (see [23] for additional details).

5.1 Analysis of edge flaws

Sidewall flaws can be idealized as edge flaws where the root geometry is not necessarily sharp. A broad range of edge flaw geometries can be modeled by a semi-superellipse defined by

$$\left(\frac{|x-x_0|}{0.5w}\right)^s + \left(\frac{|y-y_0|}{d}\right)^s = 1 \tag{5}$$

where the center of the flaw (x_0, y_0) resides on the mean surface, w is the flaw width, and d is the flaw depth. The powers s determine if the flaw is concave ($s < 1$), linear ($s = 1$), or convex ($s > 1$). The edge flaw is assumed to lie along the stress-free edge of a linear elastic, isotropic tensile bar with elastic properties chosen to be representative of a random aggregate of columnar silicon crystals where one axis of the crystal's cubic symmetry is taken to be aligned with the long axis of the columnar grain structure (E=156 GPa, ν=0.22, see Appendix C). The tensile bar is assumed to be large compared to the flaw geometry eliminating finite specimen geometry effects.

A plane strain, cohesive zone-based, finite element fracture analysis was used to predict the tensile strength of a bar containing an edge flaw with a geometry as defined by Eq. 5. The key parameters in the cohesive zone failure model are toughness K_{IC} and strength σ_{max} [24]. A polySi toughness of K_{IC}=1 MPa-m$^{1/2}$ was used in the calculations [20] while a range of strength values were considered with σ_{max} = E/5, E/7.5, and E/10 [25-26]. The value of σ_{max} affects the size of the process zone in front of a flaw, and for a sharp crack the process zone length decreases from 2.9 nm to 0.7 nm as σ_{max} ranges from E/10 to E/5. For $s = 1.5$, the material strength plays a larger role and substantial deviations from a sharp-crack, linear elastic fracture mechanics (LEFM) prediction can occur at larger flaw w/d and higher values of σ_{max} because the stress concentration is insufficient to satisfy the strength over a length scale influenced by the toughness [27]. Figure 15a plots results for σ_{max} = E/10 and s=1.5 that show how predicted tensile strength varies with root radius and flaw depth. The Fig. 15a results are interpolated and extrapolated and then normalized with respect to the LEFM prediction for a sharp crack with the same depth in Fig. 15b. This plot highlights differences in cohesive zone-based strength predictions and LEFM predictions when E/10 and $s = 1.5$. As the root radius of curvature increases, the

cohesive zone-based analysis predicts an increasingly higher strength relative to that predicted by a LEFM analysis. The deviation is modest (±10%) when the root radius of curvature is <5 nm.

As discussed in Section 3.3, every sidewall flaw in an AFM image can be defined in terms of its depth and root radius (Figs. 10-11). Moreover, the cohesive zone failure analysis defines tensile strength as a function of flaw depth and root radius (Fig. 15b). Therefore, a local strength value can be assigned to each point where there is a flaw (position where there is a local minimum in the depth profile). The region with the lowest predicted strength would be the position where failure is expected to initiate and it is this strength value that defines the sidewall strength. Implicit in this approach is the assumption that 1) edge flaws are spaced sufficiently far apart that interaction effects are limited, and 2) a 2-D, plane strain analysis of a flaw subjected to a pure Mode I loading can be used to describe the local stress state along a non-straight sidewall groove.

5.2. Predicted tensile strength of Poly3 and Poly4 sidewalls

Figure 16 plots the surface depth relative to a least-squares reference plane as obtained from AFM images of four different Poly3 sidewalls. Plotted on top of these images are the predicted local strengths. This is done for all flaws having substantial depth and curvature (d>15 nm and ρ<13 nm) so as to accentuate the most critical flaws. It is clear that the regions of lowest predicted strength are associated with grain boundary grooves. The section of a grain boundary groove with the lowest predicted strength defines the strength controlling flaw in a scanned sidewall (provided that this is not an isolated low strength point, but instead adjacent to multiple points with a similar low strength). The predicted strengths of sidewalls D5, E6, D10, and E10 are 2.8 GPa, 2.8 GPa, 2.9 GPa and 2.5 GPa, respectively (with flaw depths of 37 nm, 37 nm, 33 nm, and 42 nm, respectively). Results for two other Poly3 (C7, C10) scans had predicted strengths of 3.0 GPa and 3.2 GPa. The root radius of the dominant flaws for the Fig. 16 sidewalls varied from 2.5-4.3 nm. The small root radius of the strength controlling flaws indicate that these flaws are almost crack-like; Fig. 15b shows that cohesive zone-based and LEFM predictions only differ by 7% when the root radius is this small. Note that major defects tend to reside near the seed layer (bottom) and might explain the fractographic evidence that traces crack initiation to the bottom corners of the bars.

As discussed earlier, poly4 layers have a significantly higher tensile strength than that of poly3 (Fig. 6). This motivated the analysis of Poly4 sidewalls (Fig. 17). The predicted strengths for D5, E6, D10, and E10 are 3.3 GPa, 3.2 GPa, 3.6 GPa, and 3.0 GPa, respectively (with defect depths of 24 nm, 28 nm, 23 nm, and 41 nm, respectively). Note that although E10's dominant flaw is 41 nm deep, its root radius is a relatively large 9 nm. This generates a more significant 21% difference between cohesive zone-based and LEFM predicted strengths. It appears that the root radius of Poly4 sidewall grain boundary grooves may not be as sharp as those in Poly3. Both flaw depth and root radius may play a role in the increased strength of Poly4.

In summary, predicted strengths for Poly3 sidewalls using an AFM/FEA coupled methodology fall within the observed range, 2.0 to 3.2 GPa, and near the mean slack-chain strength of 2.7 GPa. The grain boundary grooves within sidewall curtains control the macroscopic strength. Furthermore, the proposed fracture sites near the seed layer align with fractography observations. The substantial curvatures observed along the grain boundaries in Poly3 permit a simplified description, fracture mechanics. Finally the observed difference in measured Poly3 and Poly4 tensile strengths is consistent with strength predictions.

6. Fracture analysis of specimens with stress concentrations

An important question confronting those who design MEMS devices is how to use measured tensile data to predict the strength of MEMS structures that contain micron-scale features that generate significant stress concentrations. A method that can place a lower bound limit on the strength of a complex MEMS structure, below which no failures occur, would be of particular interest when designing a highly reliable structure. This issue motivated the testing of double edge-notched (DEN) specimens that were fabricated with ~0.6 μm radius U-notches. Figure 18 shows the specimen geometry and a finite element analysis of the specimen determined that the notch-tip stress concentration factor (SCF) is 2.75 (applied to net-section stress). The SUMMiT V^{TM} polySi microfabrication process was found to produce DENs with good dimensional control. SEM images of 40 DEN specimens showed the average measured ligament width was 4.33 μm (0.03-μm standard deviation) with a minimum width of 4.28 μm and a maximum width of 4.37 μm, while the average notch-tip radius was 0.58 μm (0.02-μm standard deviation) with a minimum width of 0.54 μm and a maximum width of 0.64 μm. A total of 331 DEN specimens from RS733 Poly3 were tested using the slack-chain sequential test method. Figure 19 plots the empirical CDF.

6.1 Strength-base failure analysis

If failure simply occurs when the local stress at the notch tip reaches a critical tensile value, the DEN strength distribution can be estimated simply by scaling the tensile strength distribution by 1/SCF (i.e., DEN ligament stress at failure = tensile strength/SCF). As expected, this simple approach yields a poor estimate of the measured DEN strength distribution because it does not account for size effects (Fig. 19). The highly stressed region in the DEN specimen is very small compared to that of a tensile bar. In the DEN specimen, only the sidewall region within a ~60° segment at the notch tip is highly stressed (stress is within ~80% of its peak value). Consequently, there are only ~3 flaws subjected to a high stress in a DEN specimen while ~100 flaws are subjected to a high stress in a tensile specimen (assuming a grain width of 0.4 μm and that there is an edge flaw associated with each grain boundary). Furthermore, the finite element analysis indicates that there is a significant stress gradient over a distance comparable to the flaw size. In the tested DEN specimen, the calculated cleavage stress is reduced to 75% of its peak value at a distance of 100 nm from the notch tip.

6.2 Weibull failure analysis

A Weibull failure analysis is often the preferred approach for estimating the strength of brittle materials [3-4]. Since the strength-controlling edge flaws for the SUMMiT V^{TM} polySi occur along the sidewalls, the estimated failure probability is determined by integrating maximum principal stress over all tensile regions of the DEN specimen's sidewall surface. Furthermore, since the 3-parameter Weibull distribution is a much better fit compared to the 2-parameter fit, the 3-parameter Weibull distribution is used in the failure analysis. Accordingly, the Weibull failure analysis performed here is based on the generalization of Eq. 1 to a non-uniform stress field,

$$P = 1 - \exp\left[-\int_A \left(\frac{\sigma - \sigma_u}{\sigma_o} \right)^m dA \right] \tag{6}$$

where *A* is sidewall area and σ_o is the Weibull material scale parameter. The parameter σ_o can be thought of as the characteristic strength for a uniformly loaded tensile specimen with unit sidewall surface area (i.e., $\sigma_o = \sigma_\theta A^{1/m}$). The Weibull parameters used in the analysis are based on the RS733-RS784 tensile strength data (Table 1) and the stress state used in the integration was determined from a finite element analysis (geometry defined in Fig. 18 with Young's modulus = 161 GPa and Poisson's ratio = 0.23). The only significant contributions to the Eq. 6 integral occurs over a ~ 60° segment at the notch tip. Elements in the highly stressed region had a 0.025 μm characteristic length scale (a mesh refinement study obtained essentially the same Weibull failure analysis results when 0.050 μm elements were used instead). The DEN's predicted CDF is compared to the empirical DEN CDF in Fig. 20. The Weibull failure analysis underestimates the measured strength. Furthermore the estimated threshold strength is only 0.65 GPa. One of the key assumptions implicit in the application of a Weibull failure analysis appears to be violated when applying this analysis to SUMMiT V^{TM} structures with stress concentrations. It is assumed that a representative population of flaws is contained within a region that is small compared to specimen dimensions and stress gradients. This assumption is almost certainly not true for micron-scale stress concentrations in polySi MEMS structures where edge flaws can have a length that is similar to that associated with stress gradients. Furthermore, it should be noted that the Weibull fit of the RS733-RS784 tensile strength data is biased towards bigger critical flaws. As was already mentioned, the slack-chain tensile specimen contains ~ 100 sidewall flaws and it is extremely unlikely that every flaw in a specimen is small.

6.3 Fracture mechanics flaw tolerance analysis

One method for making a worst-case, lower bound estimate for the strength of a complex MEMS structure is to use a LEFM, flaw tolerance approach. In this approach one assumes that the largest flaw that could ever exist is located it in the most highly stressed region in a direction normal to the first principal stress. Then a LEFM analysis is performed using the estimated material toughness to determine the limit stress level below which the crack does not propagate. This approach requires that an upper bound to

flaw size exists. Fortunately, that is the case for SUMMiT V^{TM} polySi. This material was shown to have a tensile strength threshold and this implies that there is a limit to the depth of strength-controlling sidewall flaws.

One way to estimate the effective depth of strength-controlling sidewall flaws is to use linear elastic fracture mechanics. As discussed in section 4.2, an edge V-notch bounded by silicon crystals can be reasonably approximated by a sharp edge crack in a homogeneous, isotropic material. Here the strength-controlling flaw is assumed to be an edge crack with K_{IC}=1 MPa-m$^{1/2}$ (rough estimate of K_{IC}, see section 4.3). Using the K_I calibration for an edge crack that is very small relative to specimen width

$$c_{cr} = \frac{1}{\pi}\left(\frac{K_{IC}}{1.122\sigma}\right)^2 \qquad (7)$$

where c_{cr} is the critical flaw depth and σ_f is tensile strength. Note that the calculated c_{cr} is an "effective" crack depth; it depends on ratio of K_{IC}/σ, and also reflects deviations in flaw geometry from the idealized sharp crack, etc. Figure 21 plots a histogram of effective critical flaw depths inferred from the RS733-784 tensile strength data using Eq. 7. The effective critical flaw depths range from 25 nm to 61 nm with an average of 35 nm. Of the estimated 1.3 x 10^5 flaws subjected to a tensile load in the 1287 RS733-RS784 tensile tests, the largest effective c_{cr} is 61 nm. This is one estimate for the maximum critical effective crack length that can exist, but there are no associated statistical bounds. Another approach is to use the confidence interval on the threshold strength determined by the 3-parameter Weibull fit of the RS733-RS784 tensile strength data. As reported in Table I, the 95% confidence interval for σ_u = [1.62 to 1.94 GPa]. Based on these values, the maximum value of c_{cr} will fall within the range of 67-96 nm.

A lower bound to the strength of the RS733 DEN specimen can be predicted by using the 95% confidence interval for σ_u to set the maximum critical flaw depth (i.e., 67-96 nm) and then performing a LEFM analysis of the DEN specimen with a crack of this length originating from the notch tip. A finite element analysis was used to determine the K_I calibration for the RS733 DEN geometry shown in Fig. 18, and this calibration is can be expressed as

$$K_I = 1.122k\sigma_{lig}\sqrt{\pi c}\,f(c/R, L/R, W/L, H/L) \qquad (8)$$

where k is the notch SCF (equals 2.75 for the RS733 DEN geometry), geometric parameters c, R, L, W, and H are defined in Fig. 18, σ_{lig} is the average ligament stress (net section stress), and the function f is defined by the polynomial fit reported in Fig 22. For c_{cr}=67-96 nm and K_{IC}=1 MPa-m$^{1/2}$, the predicted lower bound net section notch strength falls within the range of 0.76-0.85 GPa. As desired, this lower bound estimate falls below the minimum observed strength of the 331 DEN samples (1.04 GPa). It is worth noting that a total of roughly 10^3 flaws were subjected to high stress in the 331 DEN tests, while roughly 1.3x10^5 flaws were highly stressed in the 1287 RS733-RS784 tensile tests used to infer the maximum $c_{cr.}$

7. Summary

Recently developed, high throughput test methods were used to measure the strength of SUMMiT V^{TM} Poly3, polycrystalline silicon tensile bars. Approximately 1300 nominally identical tensile bars were tested. One important finding is that measured tensile strength distributions display a strength threshold. This implies that the strength-controlling flaws produced by the SUMMiT V^{TM} microfabrication process are all less than some maximum size. In addition to sidewall edge flaws, which are clearly linked to the measured variability in tensile strength, several other potential factors were investigated. These included variations in line width, stress inhomogeneity within a polycrystal, and variations in the apparent fracture toughness. None of these appear to be a dominate contributor to tensile strength variability. The dominate nature of sidewall flaws was further confirmed by an analysis that applied cohesive zone finite element results for blunted V-notches to actual AFM-images. This analysis predicted tensile strengths for the imaged sidewalls that fell within the range of measured tensile strengths. The existence of a maximum flaw size enables the use of a flaw tolerance fracture mechanics methodology for analyzing complex MEMS structures containing micron-scale stress concentrations. This approach was used to estimate a lower bound for the strength of a double edge-notch specimen that compared favorably with measured values.

8. References

1. Boyce, B.L., et al., *Strength Distributions in Polycrystalline Silicon MEMS.* Journal of Microelectromechanical Systems, 2007. **16**: p. 170-190.
2. Chasiotis, I. and W.G. Knauss, *The mechanical strength of polysilicon films:Part 2. Size effects associated with elliptical and circular perforations.* Journal of the Mechanics and Physics of Solids, 2003. **51**: p. 1551-1572.
3. Ashby, M.F. and D.R.H. Jones, *Engineering Materials 2.* 2006, Oxford: Butterworth-Heinemann.
4. ASTM, *C1683-08: Standard Practice for Size Scaling of Tensile Strengths Using Weibull Statistics for Advanced Ceramics.* 2008, ASTM International: West Conshohocken, PA.
5. Sharpe, W.N., et al., *Fracture Strength of Silicon Carbide Microspecimens.* Journal of Microelectromechanical Systems, 2005. **14**: p. 903-913.
6. McCarty, A. and I. Chasiotis, *Description of brittle failure of non-uniform MEMS geometries.* Thin Solid Films, 2007. **515**: p. 3267-3276.
7. Greek, S., et al., *In situ tensile strength measurement and Weibull analysis of thick film and thin film micromachined polysilicon structures.* Thin Solid Films, 1997. **292**(1-2): p. 247-254.
8. Tsuchiya, T., et al., *Specimen size effect of tensile strength of surface-micromachined polycrystalline silicon thin films.* Journal of Microelectromechanical Systems, 1998. **7**(1): p. 106-113.
9. Corigliano, A., et al., *Mechanical characterization of polysilicon through on-chip tensile tests.* Journal of Microelectromechanical Systems, 2004. **13**(2): p. 200-219.
10. Alan, T., et al., *Methyl monolayers improve the fracture strength and durability of silicon nanobeams.* Applied Physics Letters, 2006. **89**(23).
11. Hazra, S.S., et al., *Demonstration of an in-situ on-chip tensile tester.* Journal of Micromechanics and Microengineering, 2009. **19**: p. 082001.
12. Boyce, B.L., *A sequential tensile method for rapid characterization of extreme-value behavior in microfabricated materials.* Experimental Mechanics, 2010.
13. Sniegowski, J.J. and M.P. de Boer, *IC-COMPATIBLE POLYSILICON SURFACE MICROMACHINING.* Annual Review of Materials Science, 2000. **30**(1): p. 299-333.
14. Breiman, L., *Statistics: With a view toward applications.* 1973, Boston: Houghton Mifflin.
15. Picu, R.C. and V. Gupta, *Singularities at Grain Triple Junctions in Two-Dimensional Polycrystals with Cubic and Orthotropic Grains.* Journal of Applied Mechanics, 1996. **63**: p. 295-300.
16. Reedy, E.D., Jr., *Singular Stress Fields at the Intersection of a Grain Boundary and a Stress-free Edge in a Columnar Polycrystal.* Journal of Applied Mechanics, 2010.
17. Ting, T.C.T., *Anisotropic Elasticity: Theory and Applications.* 1996: Oxford University Press.

18. Williams, M.L., *Stress singularities resulting from various boundary conditions in angular corners of plates in extension.* Journal of Applied Mechanics, 1952. **19**: p. 526-528.

19. Ballarini, R., R.L. Mullen, and A.H. Heuer, *The effects of heterogeneity and anisotropy on the size effect in cracked polycrystalline films.* International Journal of Fracture, 1999. **95**: p. 19-39.

20. Chasiotis, I., S.W. Cho, and K. Jonnalagadda, *Fracture Toughness and Subcritical Crack Growth in Polycrystalline Silicon.* Journal of Applied Mechanics, 2006. **73**: p. 714-722.

21. Chen, C.P. and M.H. Leipold, *Fracture Toughness of Silicon.* American Ceramic Society Bulletin, 1980. **59**: p. 469-472.

22. Yasutake, K., et al., *Crack healing and fracture strength of silicon crystals.* Journal of Materials Science, 1986. **21**: p. 2185-2192.

23. Foulk III, J.W., et al., *Developing a methodology for measuring and predicting dominant edge flaws in brittle materials.* in preparation.

24. Tvergaard, V. and J.W. Hutchinson, *The influence of plasticity on mixed mode interface toughness.* Journal of the Mechanics and Physics of Solids, 1993. **41**: p. 1119-1135.

25. Umeno, Y., et al., *Ab initio study of the surface properties and ideal strength of (100)silicon thin films* Physical Review B, 2005. **72**: p. 165431-1 – 165431-7.

26. Macmillan, N.H., *Review: The theoretical strength of solids.* Journal of Materials Science, 1972. **7**: p. 239-254.

27. Foulk III, J.W., et al., *On the toughening of brittle materials by grain bridging: Promoting intergranular fracture through grain angle, strength, and toughness.* Journal of the Mechanics and Physics of Solids, 2008. **56**: p. 2381-2400.

9. Tables

Table 1. Three-parameter Weibull fit parameters m, σ_θ, and σ_u along with their 95% confidence intervals (CI); n denotes the number of specimens tested.

	n	m	m 95% CI	σ_θ (GPa)	σ_θ (GPa) 95% CI	σ_u (GPa)	σ_u (GPa) 95% CI
RS686[1] [12]	1008	7.73	5.66-10.54	1.23	0.92-1.66	1.40	1.04-1.76
RS733	616	6.20	4.65-8.26	1.08	0.83-1.41	1.70	1.41-1.98
RS784	671	5.48	4.44-6.77	0.92	0.76-1.12	1.84	1.67-2.01
RS733-RS784	1287	5.78	4.85-6.88	0.99	0.84-1.16	1.78	1.62-1.94
RS784-OC	231	3.03	2.39-3.84	0.52	0.43-0.62	2.08	1.99-2.17
RS733-P4	591	6.24	4.66-8.35	1.74	1.33-2.29	2.10	1.64-2.56

[1] specimen with 1.9 μm x 2.33 μm cross-section

10. Figures

a)   b)
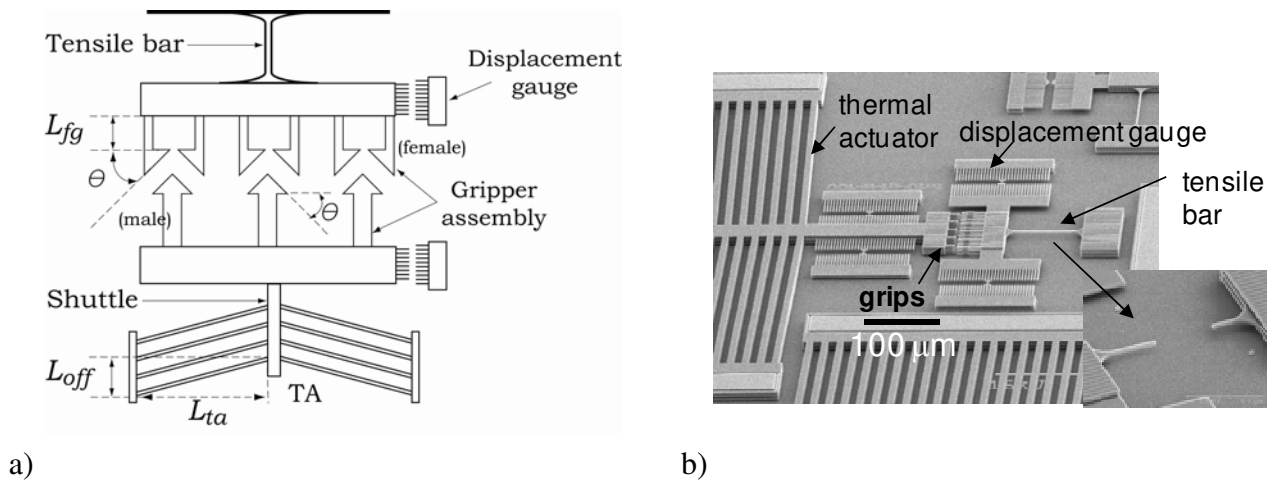
Fig. 1. On-chip tensile tester, a) schematic and b) SEM of tester.

a)

b)
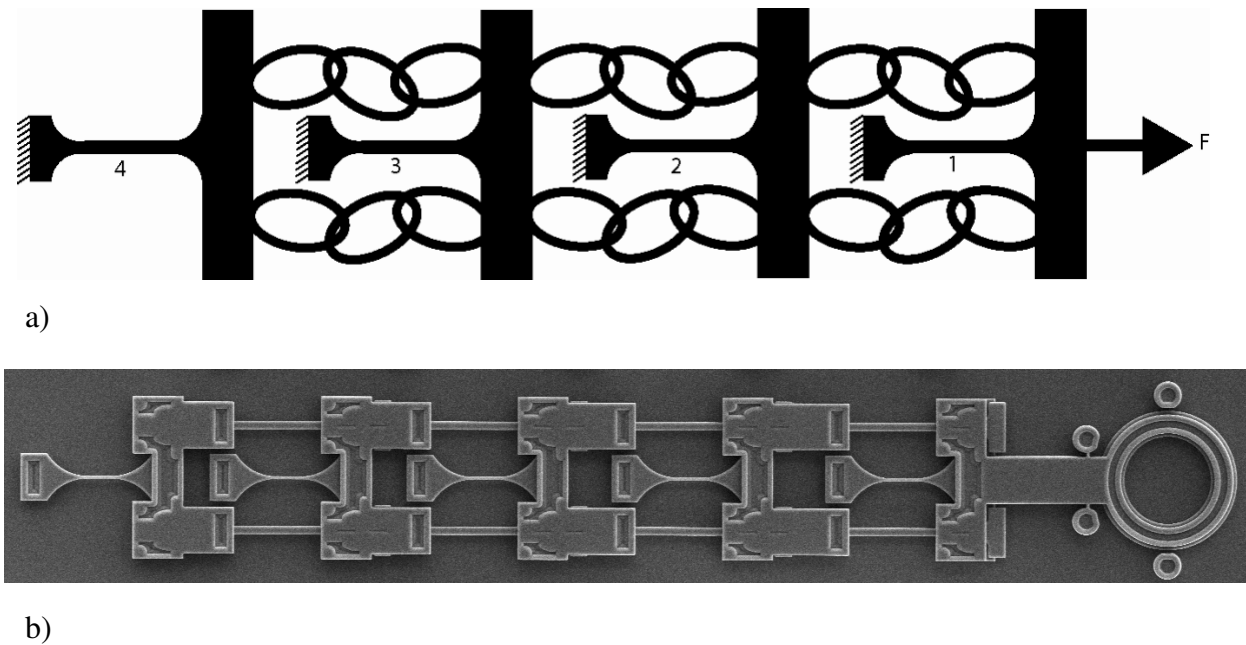
Fig. 2. Slack-chain tensile tester, a) schematic and b) SEM of portion of one chain.

27
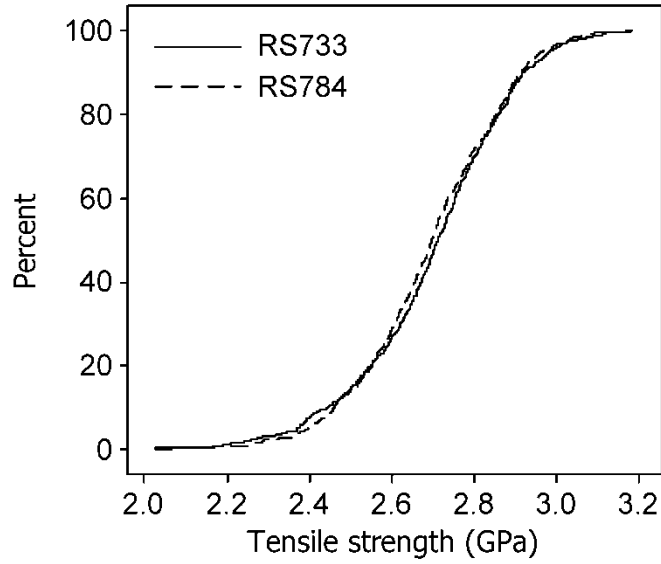
Fig. 3.Empicial CDF of the strength of RS733 and RS784 tensile bars measured using the slack-chain method.
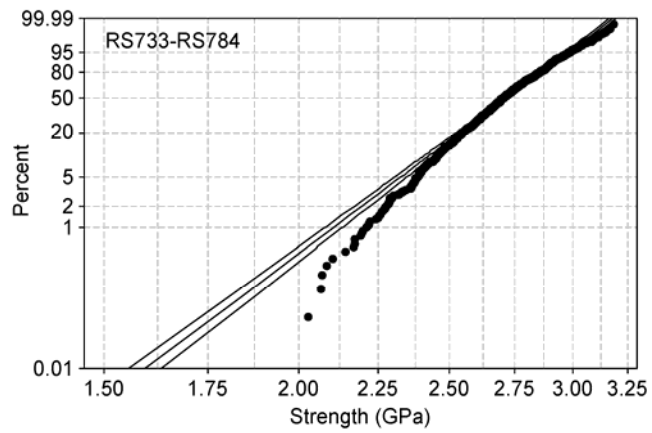
Fig. 4. Slack-chain RS733-RS784 tensile strength data plotted along with 2-parameter Weibull fit (95% CI shown).
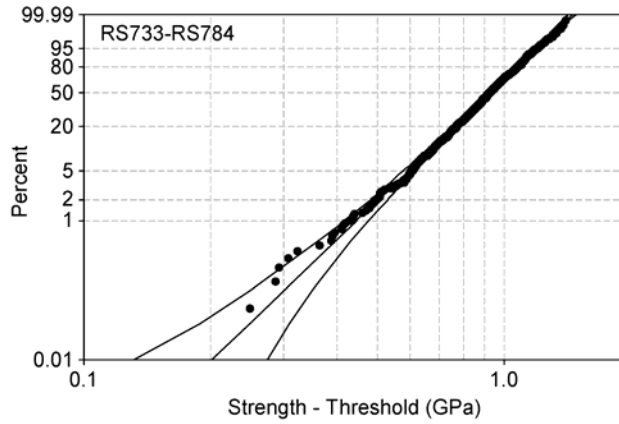
Fig. 5. Slack-chain RS733-RS784 tensile strength data plotted along with 3-parameter Weibull fit (95% CI shown).
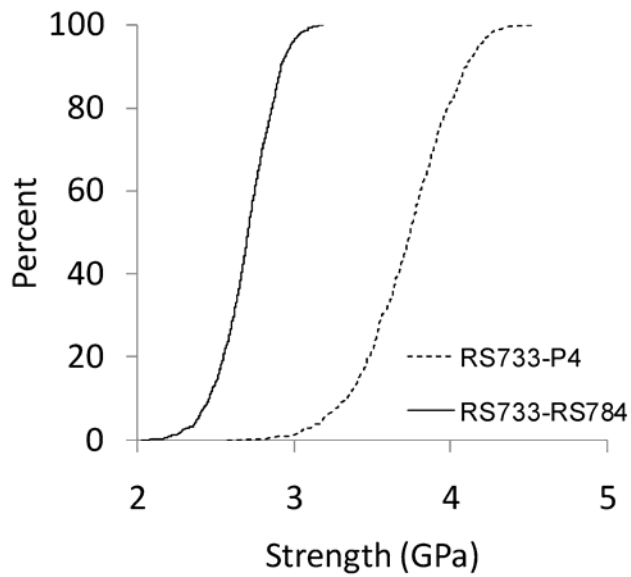
Fig. 6. Empirical CDF of the strength of RS733-P4 Poly4 tensile bars compared with that of RS733-RS784 Poly3 tensile bars.
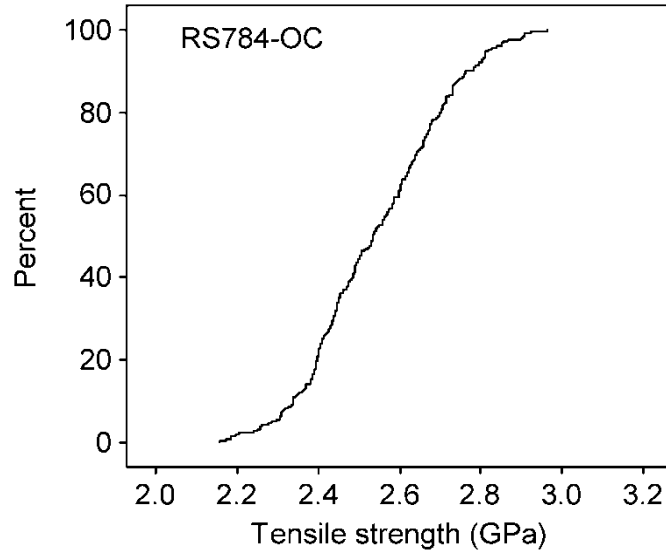
Fig. 7. Empirical CDF of the strength RS784-OC tensile bars measured using the on-chip method.
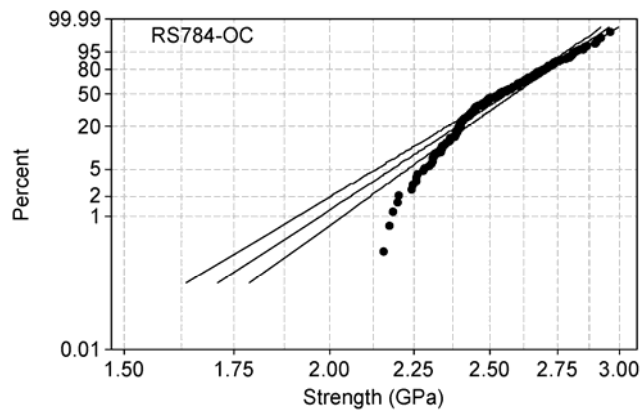
Fig. 8. On-chip RS784-OC tensile strength data plotted along with 2-parameter Weibull fit (95% CI shown).
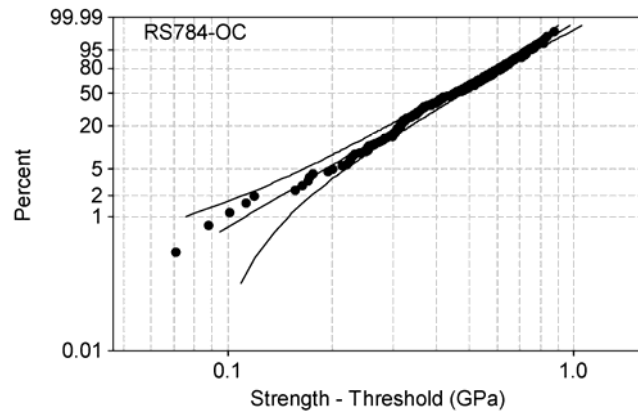
Fig. 9. On-chip RS784-OC tensile strength data plotted along with 3-parameter Weibull fit (95% CI shown).
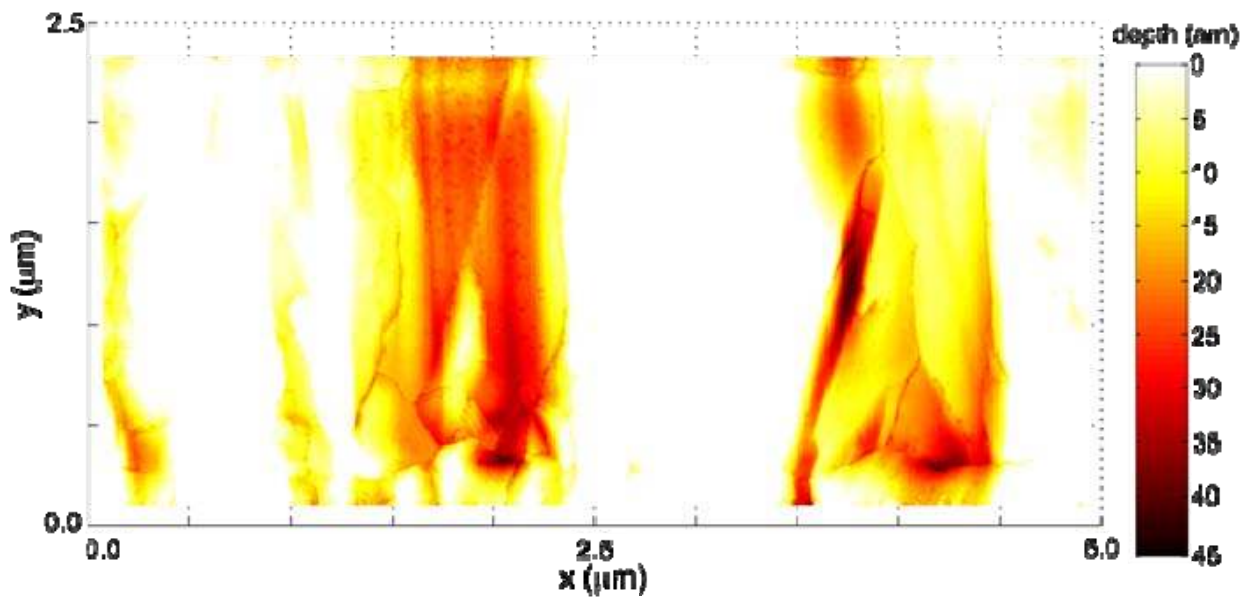
Fig. 10. Surface depth of a Poly3 sidewall relative to a least-squares reference plane as determined by a fit of raw AFM data. (2.5 μm by 5.0 μm region).
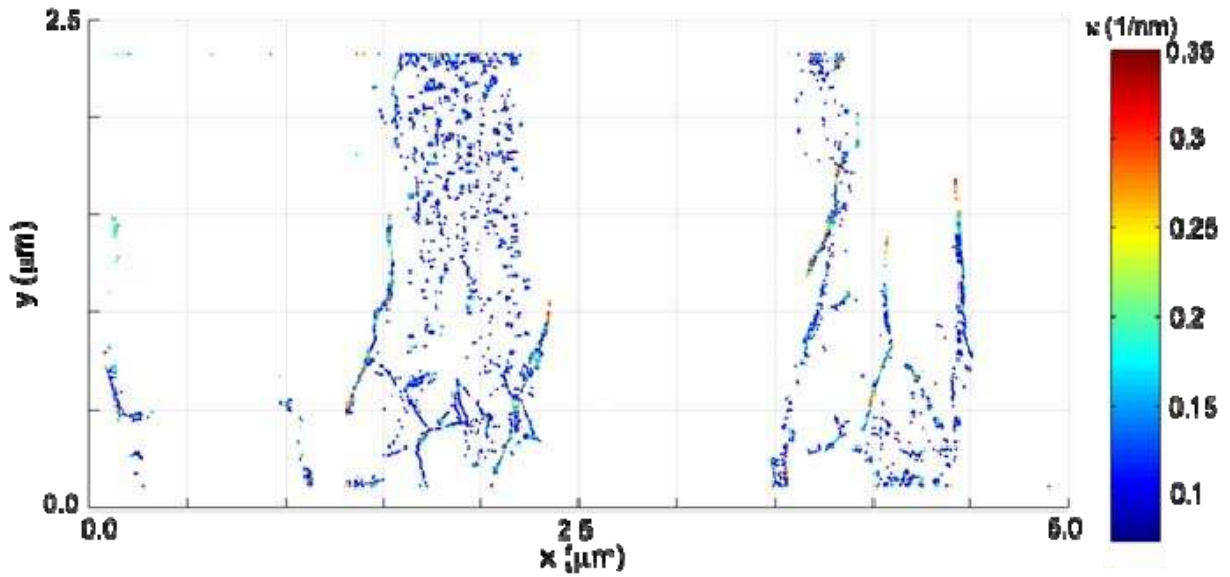
Fig. 11. Plot of curvature determined from the AFM image shown in Fig. 10. Surface minima of substantial depth d > 15 nm and curvature κ > 0.075 nm^{-1} lie along the grain boundaries.
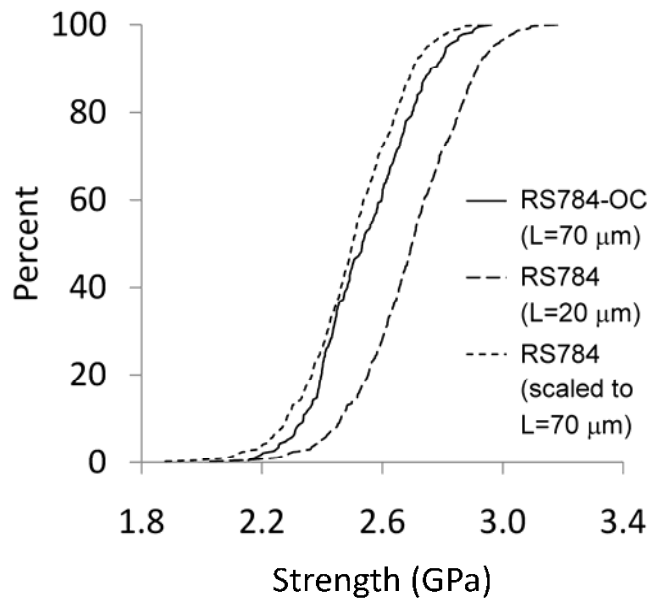
Fig. 12. Comparison of RS784-OC (L=70μm) empirical CDF with RS784 (L=20 μm) empirical CDF as well as estimated CDF of RS784 for L=70 μm.
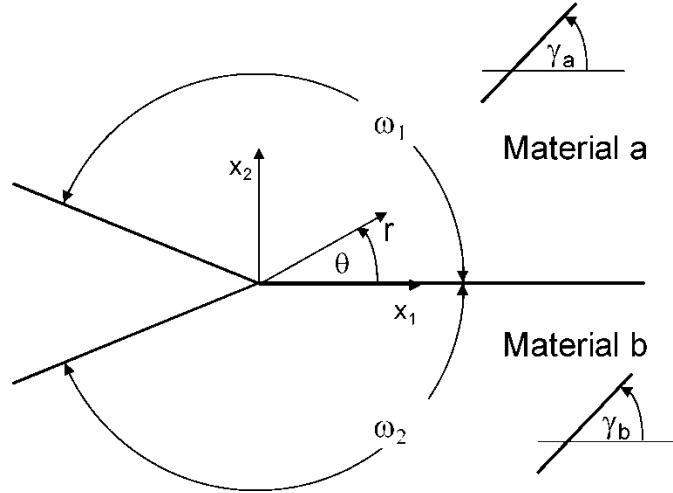
Fig. 13. Asymptotic problem for a sharp V-notch between two silicon crystals with orientations γ_a and γ_b.
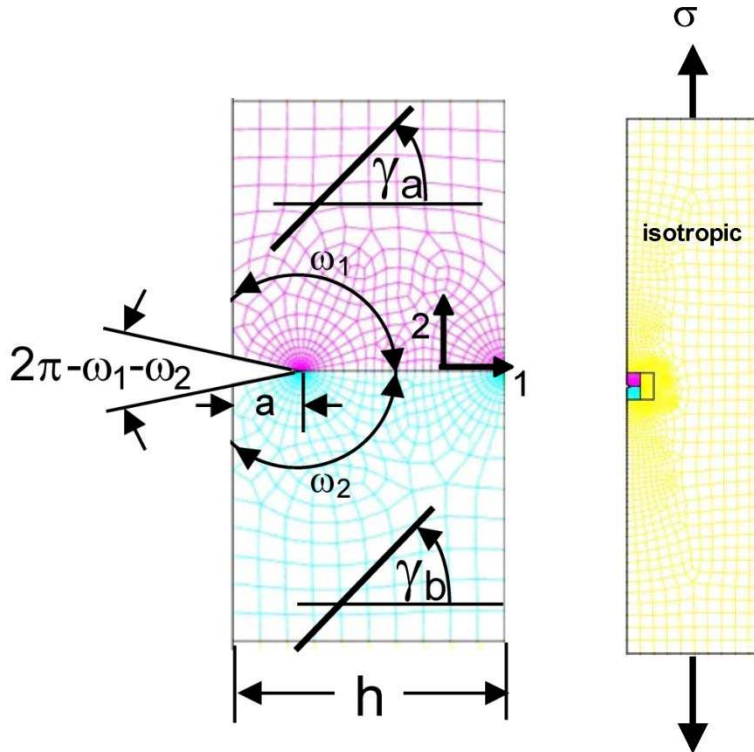
Fig. 14. Idealized problem of an edge V-notch in a tensile bar where the three silicon crystals in the immediate vicinity of the V-notch are modeled explicitly.
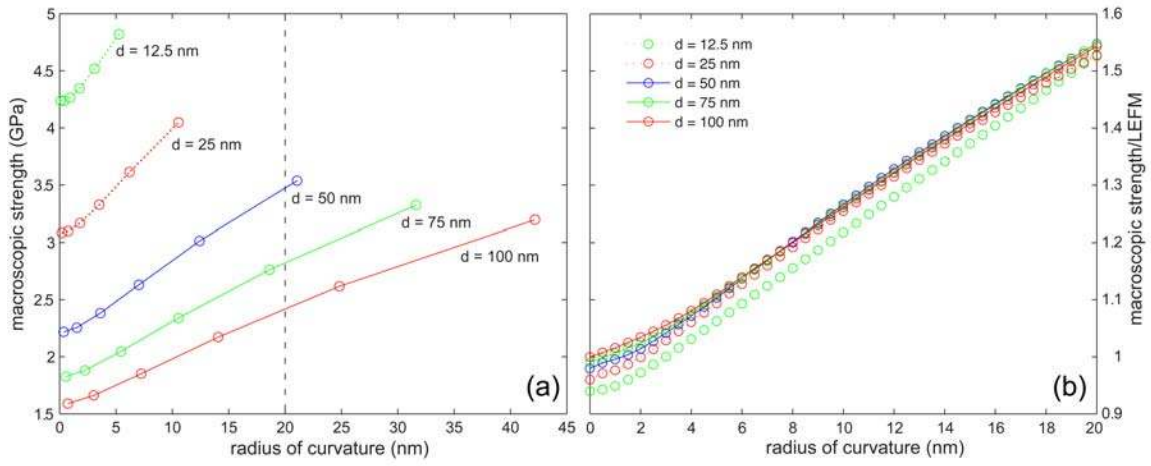
Fig. 15. Predicted tensile strength a) as a function of depth and root radius and (b) tensile strength normalized by LEFM solution for a crack of the same depth as a function of root radius ($\sigma_{max} = E/10$, $s = 1.5$).
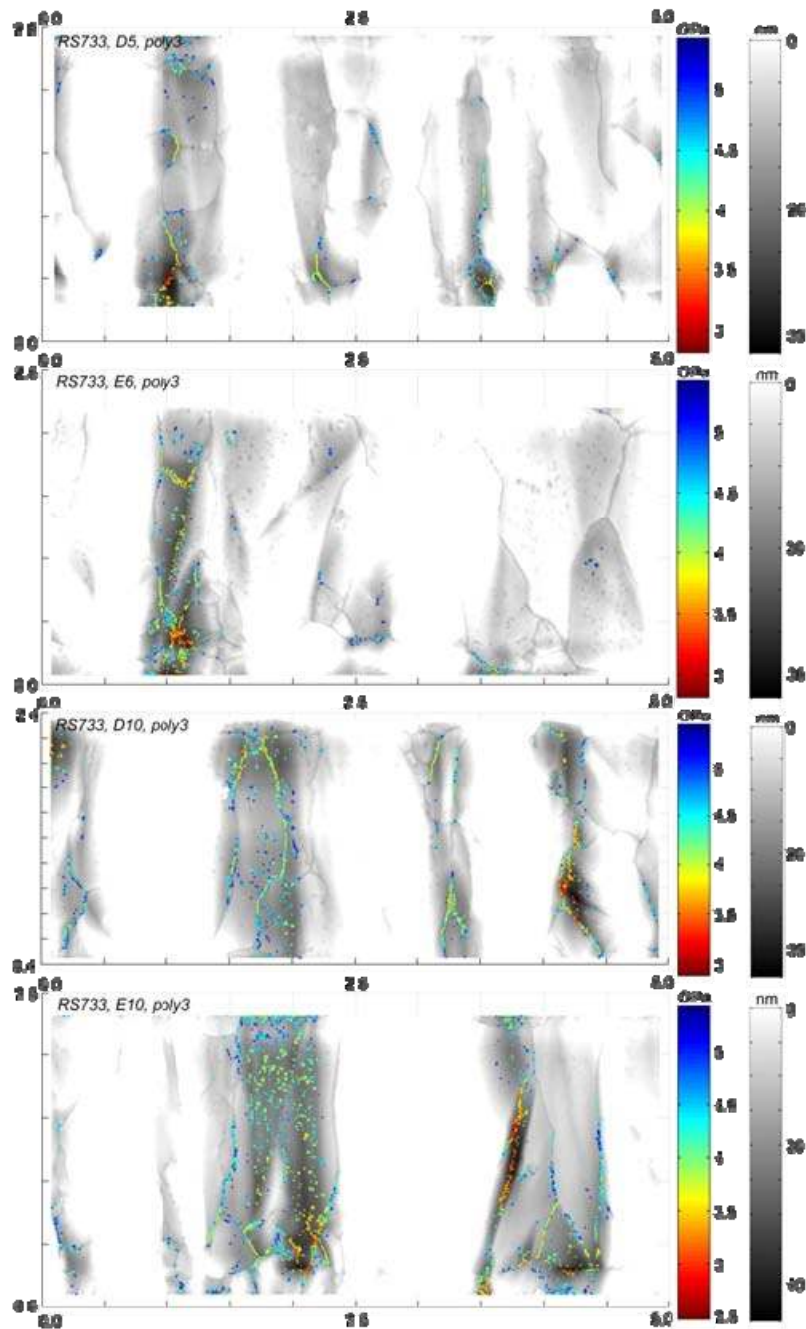
Fig. 16. Surface depths (in nm) of nominally 2.5 µm x 5.0 µm regions of the Poly3 sidewall along with predicted local strengths (in GPa) for d>15 nm and ρ<13 nm. The predicted strengths of D5, E6, D10, and E10 are 2.8 GPa, 2.8 GPa, 2.9 GPa and 2.5 GPa, respectively.
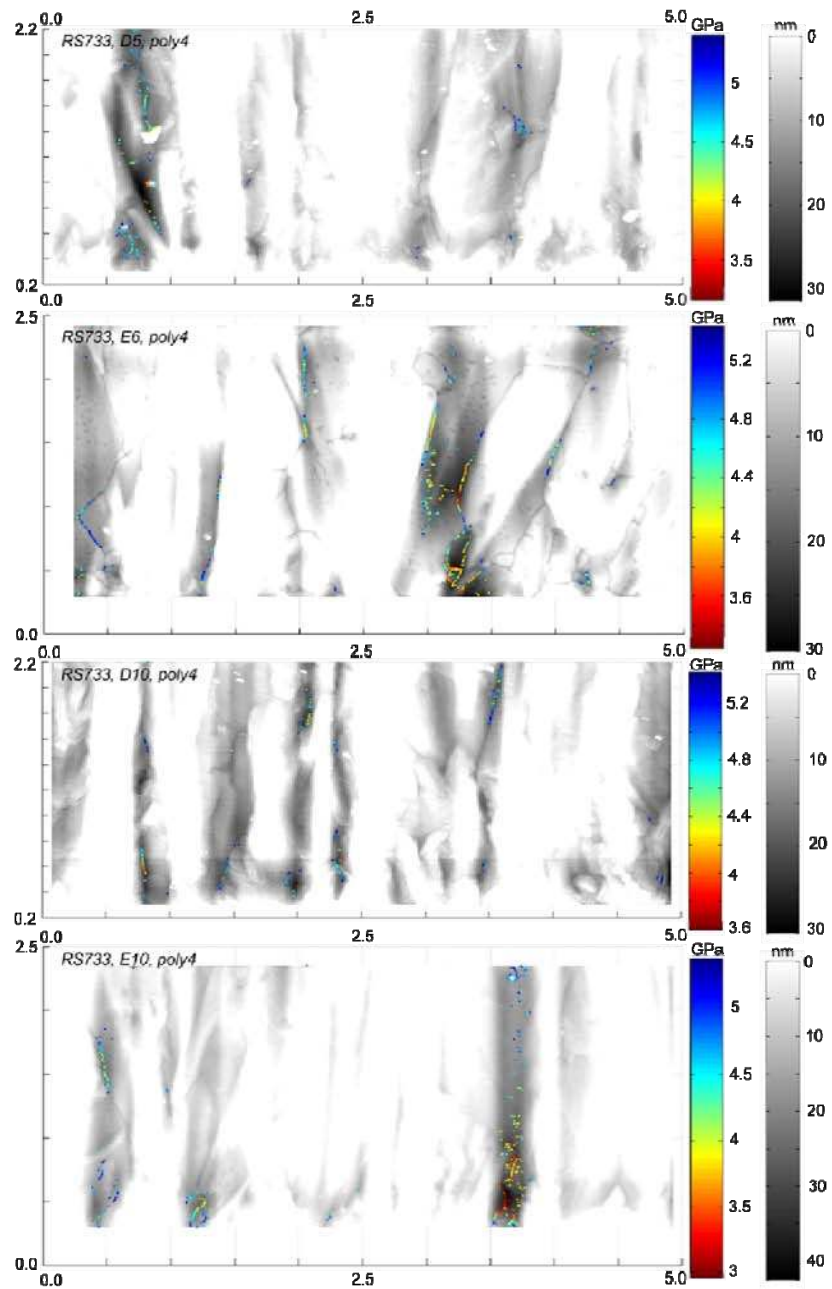
Fig. 17. Surface depths (in nm) of nominally 2.5 μm x 5.0 μm regions of the Poly4 sidewall along with predicted local strengths (in GPa) for d>15 nm and ρ<13 nm. The predicted strengths of D5, E6, D10, and E10 are 3.4 GPa, 3.2 GPa, 3.6 GPa and 3.0 GPa, respectively.
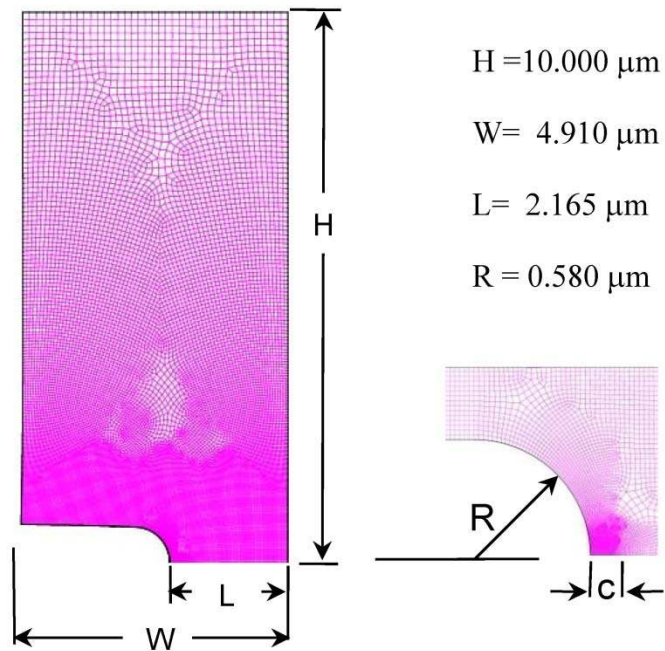
Fig. 18. Finite element mesh showing geometry of the Double Edge Notched (DEN) RS733 specimen that was tested and analyzed (shows one-quarter of specimen; symmetric about bottom and right-hand side edges).
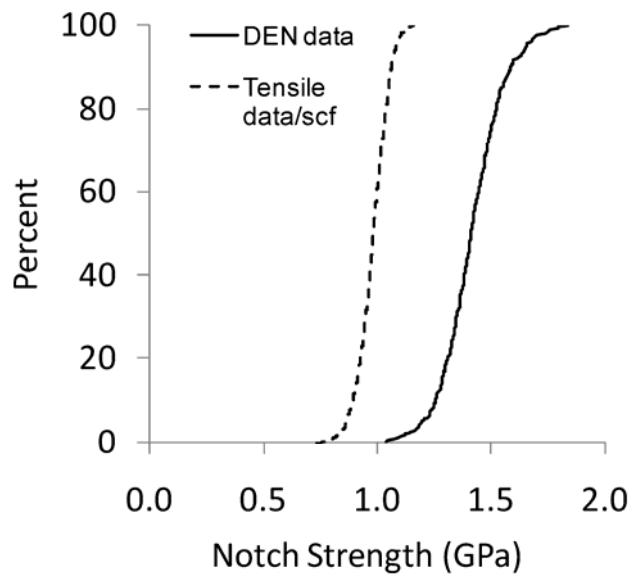
Fig. 19. Empirical CDF of RS733 DEN specimen compared with prediction based on the notch-tip stress equaling a critical tensile value.
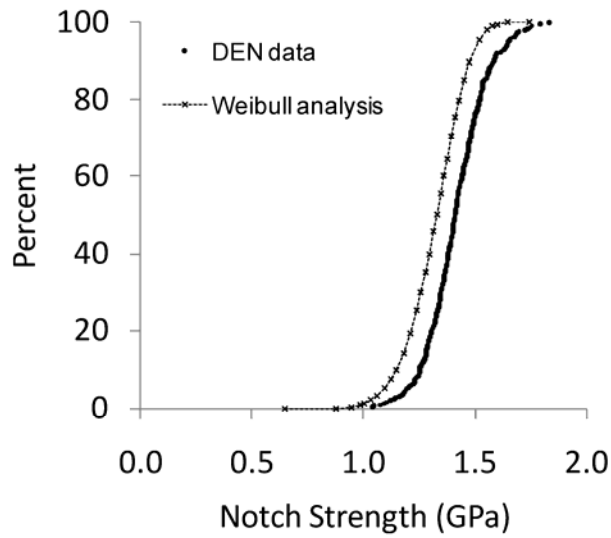
Fig. 20. Empirical CDF of RS733 DEN specimen compared with that of a 3-parameter Weibull failure analysis prediction.
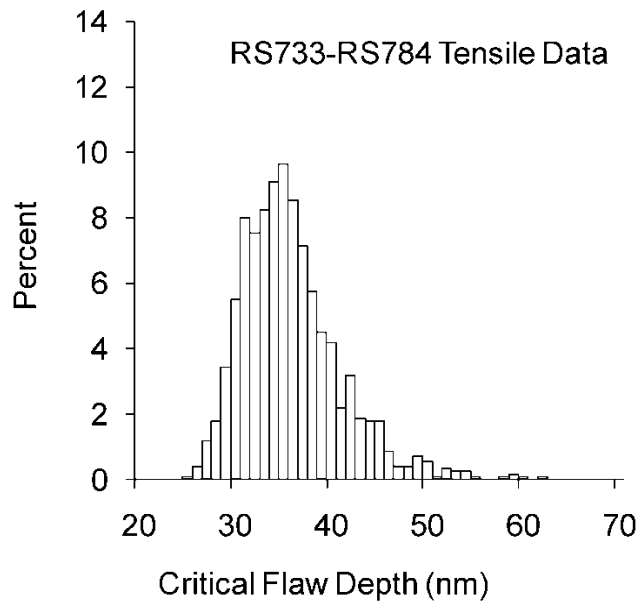
Fig. 21. Histogram of effective critical flaw depths inferred from RS733-784 tensile strength data.
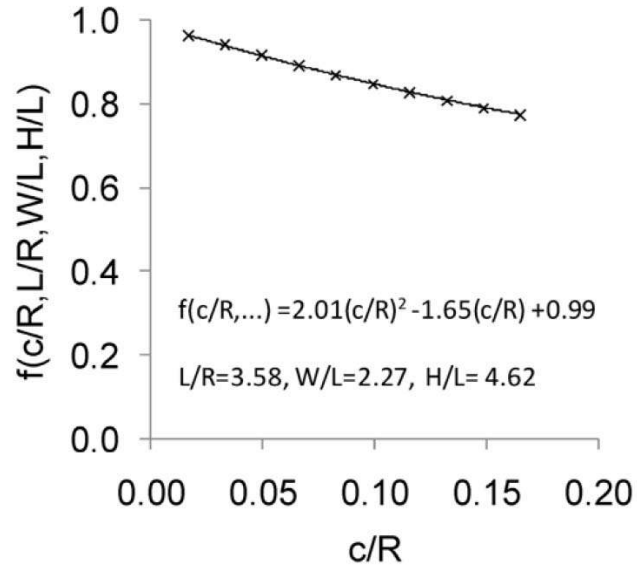
Fig. 22. K-calibration for the DEN specimen shown in Fig. 18.

11. Appendix A: Fractographic evidence of crack origins

Fractography, or analysis of microscope images of fracture surfaces, is a common tool employed by metallurgists and ceramists to infer many aspects of failure: the initiation site for the crack or native flaw, the direction and extent of crack propagation, in some cases the rate of crack propagation, and even the stress state which drove cracking. In the case of brittle fracture, three characteristic regions are typically associated with the fracture surface: mirror, mist, and hackle. These regions are most easily identified in the fracture of brittle amorphous materials such as glass, since there are no other features present to confound interpretation. In the fracture of brittle polycrystalline materials, the investigator must identify the characteristic regions even though they are superimposed on the complex faceting associated with multiple crystallographic cleavage planes. This deconvolution is often tractable because in conventional-scale brittle components the grain structure is much finer than the size of the mirror, mist, and hackle regions. However, in brittle polycrystalline microsystems, there are only a handful of grains through the thickness of the component. This makes correct interpretation of the mirror, mist, and hackle regions exceptionally challenging and correct identification of the failure location can become more subjective. To further complicate matters, the entire fracture surface is very small, on the order of a few microns, and must be imaged with high quality electron optics. Finally, the poorly conducting polysilicon material and the non-conducting nitride and oxide layers additionally challenge the electron microscopy effort. Even under the best of conditions, there is significant image distortion (due to scan drift) and blurring (due to charging).

Fractographic images were obtained using two scanning electron microscopes: a Zeiss Supra 55VP and an FEI Magellan. Accelerating voltages in the range of 1-5 keV were chosen to keep the electron-matter interaction volume minimized. Images were collected using either and Everhardt-Thornley or In-Lens detector. Several examples of fracture surface images are shown in Figure A1.

In previous studies, only a handful of fractographic images were collected and interpreted. The images confirmed that the crack origins were at the surface of the polysilcon rather than in the interior of the sample. There was also the suggestion that the failure location was mostly associated with the sidewalls and corners of the specimen. However, there was an occasional image that showed failure either at the top or bottom surface of the tensile bar, such as shown in Figure A1a. Yet, there were not enough images to assess the prevalence of various failure locations in a quantitative way.

To permit quantitative assessment of the prevalence of crack origin locations in polysilicon, over 400 fractographic images were collected. These images were taken from broken slack-chain poly3 tensile bars from reticle set RS784. About half were coated with vapor-phase self-assembled monolayer (VSAM) and half were not. Of the 400 images collected, 245 could be associated with a reasonably clear failure origin location. The resulting prevalence of failure locations is shown in Figure A2. Failure locations were associated with one of eight locations. When the crack origin was close to one corner (within ~100 nm of the corner), it was ascribed as a failure event associated with that corner. When the crack origin was close to one of the sides or top or bottom surface but not close to a corner, it was associated with that particular surface.
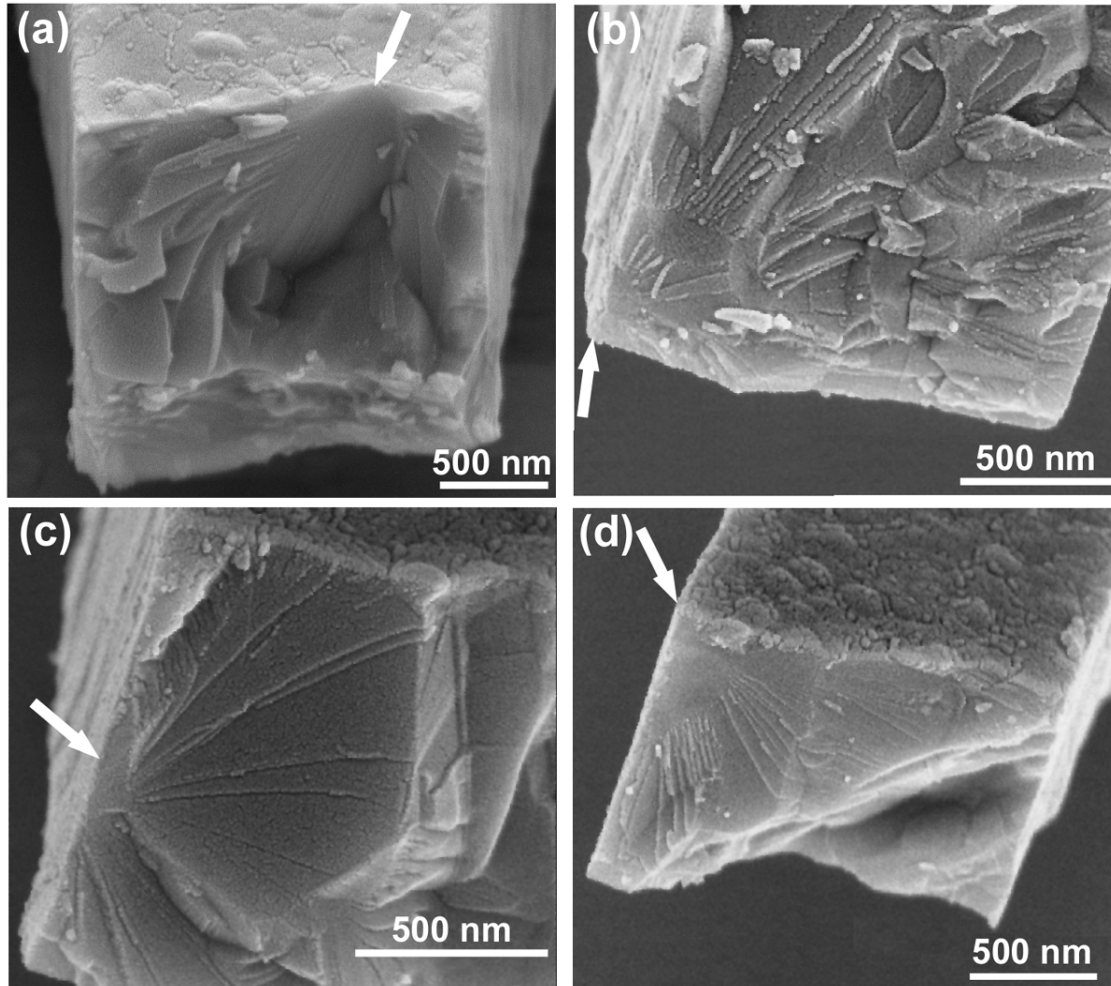
Figure A1. Fracture surfaces from poly21 (a and b), and poly2 (c and d) showing apparent evidence of failure origins [arrows] at sidewalls (c), top surfaces (a), and corners (b and d). Many other fractographs had no clearly identifiable fracture origin.

From these 245 images, none of the failures were associated with the middle of the top surface or the middle of the bottom surface. They were all associated with the sidewalls or corners. Previous observations had occasionally identified a top surface or bottom surface failure (see Figure A1a), albeit rare. The present study suggests that the probability of a failure being associated with a top or bottom surface is <0.3%! The bottom corners were clearly the preferred crack origin location, representing 69% of all of the observations. There are two possible explanations for the dominance of bottm conrer failures: (1) the samples were not loaded in pure tension but instead had a significant bending component leading to excess tensile stress on the bottom surface, or (2) the processing method produces most critical defects at these locations. Based on discussions with SUMMiT V fabrication specialists, we suspect that the etch release process is responsible for the most significant defects being present at the bottom corners of the tensile bar.
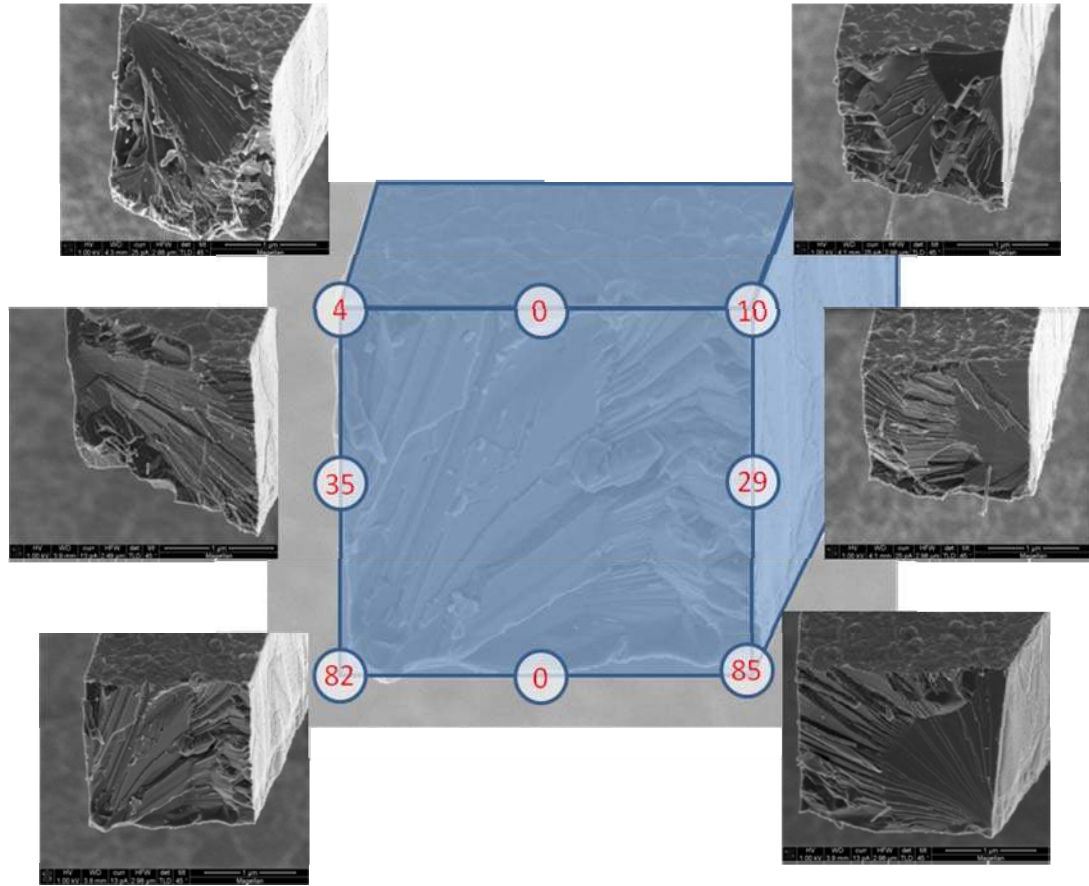
Figure A2. Prevalence of failure locations indicated by red numbers corresponding to the number of failures associated with that origin location.

12. Appendix B: Details on linewidth measurements

One of the sources of variability in the fracture behavior of MEMS polysilicon is geometric variability associated with the tested component.   The primary geometric sources of variability in a tensile bar are width and thickness. Length of the tensile bar is a less important factor because to first order it doesn't have a strong influence on the fracture force (setting aside the Weibull size effect), and because the length of the present tensile bars were much larger than the width or thickness values, and hence more repeatable. The present study focused largely on variations in tensile bar width (also called line width) rather than thickness. Thickness was thought to be a more carefully controlled dimension, due to the planarization step in the processing of polysilicon. This assertion was consistent with parametric monitoring data which suggested that thickness was more repeatable than line width.

In early studies on polysilicon, the line width was assumed to be equal to the intended design value. In other words, if a tensile bar was drawn to have a width of 2 microns in the autocad layout, all tensile bars of that geometry were assumed to have a 2 micron width. This had significant impact on the subsequent force-over-area calculations, since the true width of the tensile bars was often 0.2 microns or more below the intended value on average due to well-known line width loss effects associated with the SUMMiT V process. More recently, when a batch of tensile tests were conducted, a handful of tensile samples from that batch were measured in an SEM, and the average width of that small sample was taken as a representative width for all of the tensile bars from that batch. While this approach could approximately correct for average line width loss issues, it still could not be use to quantitatively assess the role of line width variability on overall fracture variability.

For this purpose, a set of 208 polysilicon tensile bars from the poly21, poly3, and poly4 layers of reticule set RS733 were measured in a FEI Magellan scanning electron microscope prior to tensile testing. On each tensile bar, typically 3-4 width measurements were performed to allow for slight waviness in the sides of the tensile bar and to allow for operator error, as shown in Figure B1. The tabulated width values for each tensile bar, along with the corresponding fracture force, and information regarding the die location, poly layer, and position ('row') in the slack-chain are included in Table B1.

There was clearly a correlation between poly layer and width: the average tensile bar width of the poly21 layer was 1.924 ± 0.020 μm, the poly3 layer was 1.729 ± 0.044 μm, and the poly4 layer was 1.410 ± 0.059 μm. There was also a clear correlation with die location. These 208 tests were associated with six die: three die from near the middle of the wafer, and three die from near the edge of the wafer. As shown in Figure B2, the die near the edge of the wafer had consistently lower line widths compared to those from the center of the wafer. This effect is likely due to aberrations in the lithography optics the vary from center to edge.

Another way to look at the line width dataset is to consider how much of an impact the line width variability had on overall fracture variability.   By regressing fracture force as a function of line width from Table B1, one can assess this impact. For each of the three layers and for the combined dataset of all three poly layers, the R^2

correlation coefficient of failure force as a function of line width was only ~8-10%. This suggests that 90% or more of the variability in fracture force was due to factors other than line width.
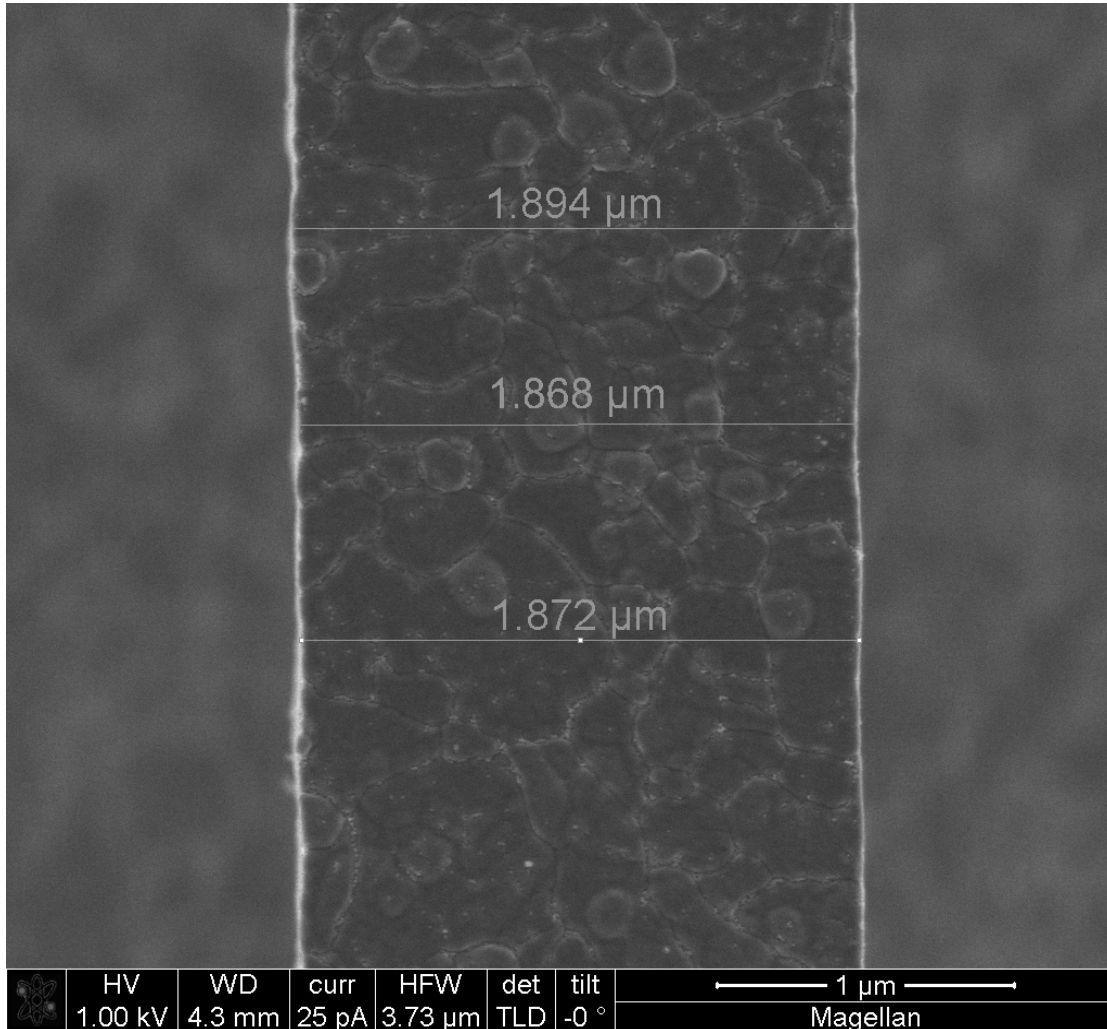
Figure B1: An example of three line width measurements taken on a single tensile bar.
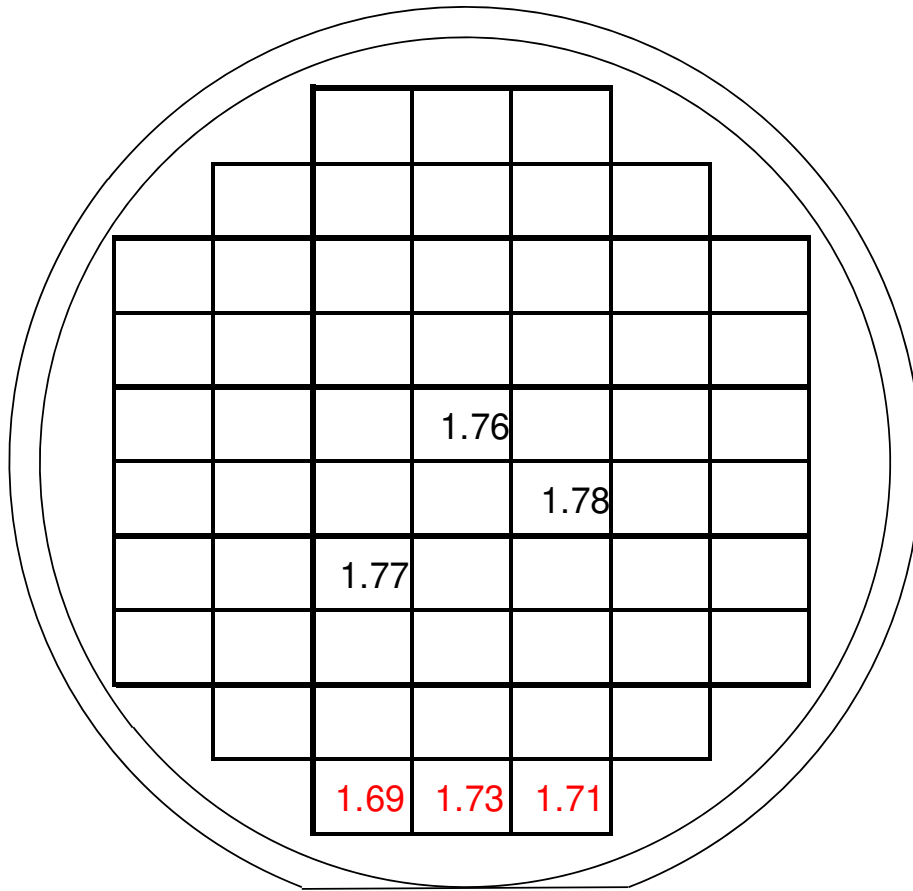
Figure B2: Average line width values for the poly3 layer of three die near the center of the wafer compared to three die near the edge of the wafer. Red values are below 1.75 μm.

Table B1: Width measurements and corresponding fracture force for 208 silicon tensile bars from 6 different die. Tensile bars from the poly21, poly3, and poly4 layers were measured and tested. All thickness and width values are in μm.

Die	Poly Layer	Row	Fracture Force (mN)	Thick-ness	width 1	width 2	width 3	width 4	average width	width standard deviation
D10	p21	1	11.79	2.39	1.929	1.920	1.923		1.924	0.005
D10	p21	2	13.03	2.39	1.929	1.915	1.938		1.927	0.012
D10	p21	3	12.5	2.39	1.929	1.920	1.917		1.922	0.006
D10	p21	5	12	2.39	1.952	1.917	1.920		1.930	0.019
D10	p21	6	11.88	2.39	1.927	1.944	1.933		1.935	0.009
D10	p21	7	12.21	2.39	1.932	1.903	1.938		1.924	0.019
D10	p21	9	12.5	2.39	1.950	1.947	1.932		1.943	0.010
D10	p21	10	12.67	2.39	1.950	1.917			1.934	0.023
E10	p21	1	11.211	2.39	1.918	1.923	1.903		1.915	0.010

E10	p21	2	10.871	2.39	1.923	1.885			1.904	0.027
E10	p21	3	12.077	2.39	1.909	1.923	1.923		1.918	0.008
E10	p21	4	12.415	2.39	1.915	1.909	1.894		1.906	0.011
E10	p21	5	12.147	2.39	1.917	1.903	1.912		1.911	0.007
E10	p21	6	12.817	2.39	1.917	1.909	1.915		1.914	0.004
E10	p21	7	11.571	2.39	1.920	1.917	1.906		1.914	0.007
E10	p21	8	10.361	2.39	1.929	1.882	1.909		1.907	0.024
E10	p21	9	11.158	2.39	1.952	1.915	1.953		1.940	0.022
E10	p21	12	12.273	2.39	1.927	1.918	1.900		1.915	0.014
E10	p21	14	12.252	2.39	1.865	1.880	1.926		1.890	0.032
E6	p21	1	12.729	2.39	1.903	1.926	1.877		1.902	0.025
E6	p21	2	13.108	2.39	1.909	1.883	1.932	1.885	1.902	0.023
E6	p21	3	11.868	2.39	1.897	1.929	1.903		1.910	0.017
E6	p21	4	12.601	2.39	1.915	1.900	1.915		1.910	0.009
E6	p21	8	13.286	2.39	1.919	1.878	1.884	1.907	1.897	0.019
E6	p21	9	13.484	2.39	1.862	1.912	1.883		1.886	0.025
E6	p21	11	12.912	2.39	1.903	1.880	1.897	1.885	1.891	0.011
E6	p21	14	12.697	2.39	1.833	1.880	1.880	1.883	1.869	0.024
C7	p21	1	12.239	2.39	1.935	1.923	1.976	1.984	1.955	0.030
C7	p21	2	12.382	2.39	1.909	1.912	1.938		1.920	0.016
C7	p21	3	12.778	2.39	1.967	1.961	1.938	1.947	1.953	0.013
C7	p21	4	13.084	2.39	1.926	1.926	1.926	1.941	1.930	0.008
C7	p21	5	12.949	2.39	1.929	1.920	1.964		1.938	0.023
C7	p21	7	12.783	2.39	1.950	1.938	1.906		1.931	0.023
C7	p21	8	13.32	2.39	1.938	1.912	1.938	1.947	1.934	0.015
C7	p21	9	11.511	2.39	1.900	1.891	1.880	1.917	1.897	0.016
C7	p21	11	12.924	2.39	1.935	1.944	1.947	1.967	1.948	0.014
C7	p21	12	12.833	2.39	1.932	1.932	1.967	1.958	1.947	0.018
C7	p21	13	12.844	2.39	1.944	1.970	1.909	1.929	1.938	0.026
C7	p21	14	12.186	2.39	1.938	1.935	1.891	1.900	1.916	0.024
C7	p21	15	13.72	2.39	1.935	1.897	1.891		1.908	0.024
D5	p21	2	13.438	2.39	1.955	1.912	1.961		1.943	0.027
D5	p21	3	12.235	2.39	1.955	1.961	1.935	1.947	1.950	0.011
D5	p21	4	12.977	2.39	1.973	1.947	1.947	1.967	1.959	0.014
D5	p21	5	12.601	2.39	1.958	1.935	1.976		1.956	0.021
D5	p21	6	11.038	2.39	1.935	1.929	1.935		1.933	0.003
D5	p21	7	12.202	2.39	1.958	1.929	1.932		1.940	0.016
D5	p21	8	12.222	2.39	1.944	1.947	1.961	1.961	1.953	0.009
D5	p21	9	13.017	2.39	1.947	1.897	1.964	1.955	1.941	0.030
D5	p21	10	13.452	2.39	1.944	1.990	1.894	1.944	1.943	0.039
D5	p21	12	11.971	2.39	1.917	1.950	1.915	1.970	1.938	0.027
D5	p21	13	11.525	2.39	1.909	1.897	1.947	1.926	1.920	0.022
D5	p21	14	12.346	2.39	1.929	1.952	1.882		1.921	0.036

D10	p3	1	9.78	2.33	1.795	1.801			1.798	0.004
D10	p3	2	10.67	2.33	1.754	1.751	1.775		1.760	0.013
D10	p3	4	9.64	2.33	1.702	1.705	1.684		1.697	0.011
D10	p3	5	8.8	2.33	1.740	1.725			1.733	0.011
D10	p3	6	10.66	2.33	1.713	1.687	1.737		1.712	0.025
D10	p3	7	11.13	2.33	1.676	1.681	1.673		1.677	0.004
D10	p3	8	10.46	2.33	1.714	1.661	1.693		1.689	0.027
D10	p3	9	10.11	2.33	1.696	1.725	1.711		1.711	0.015
D10	p3	10	10.07	2.33	1.693	1.684	1.687		1.688	0.005
D10	p3	11	10.2	2.33	1.758	1.750	1.758		1.755	0.005
D10	p3	12	9.77	2.33	1.696	1.673	1.681		1.683	0.012
D10	p3	13	9.61	2.33	1.780	1.760	1.783		1.774	0.013
D10	p3	14	10.25	2.33	1.807	1.813	1.830		1.817	0.012
D10	p3	15	10.27	2.33	1.746	1.760	1.772		1.759	0.013
E10	p3	1	8.394	2.33	1.702	1.687	1.667		1.685	0.018
E10	p3	3	8.372	2.33	1.690	1.708	1.679		1.692	0.015
E10	p3	4	9.963	2.33	1.748	1.769	1.746		1.754	0.013
E10	p3	5	9.398	2.33	1.760	1.763	1.731		1.751	0.018
E10	p3	6	10.035	2.33	1.763	1.772	1.775		1.770	0.006
E10	p3	7	9.784	2.33	1.673	1.693	1.734		1.700	0.031
E10	p3	8	8.518	2.33	1.664	1.667	1.661		1.664	0.003
E10	p3	9	9.67	2.33	1.661	1.681			1.671	0.014
E10	p3	11	11.077	2.33	1.681	1.664	1.670		1.672	0.009
E10	p3	13	10.052	2.33	1.687	1.702	1.696		1.695	0.008
E10	p3	14	9.694	2.33	1.731	1.696	1.699		1.709	0.019
E10	p3	15	10.815	2.33	1.725	1.734	1.734		1.731	0.005
C10	p3	3	8.986	2.33	1.670	1.664	1.687		1.674	0.012
C10	p3	4	11.072	2.33	1.757	1.746	1.763		1.755	0.009
C10	p3	5	10.842	2.33	1.681	1.679	1.687		1.682	0.004
C10	p3	6	10.029	2.33	1.711	1.632	1.623		1.655	0.048
C10	p3	7	9.5	2.33	1.664	1.681	1.655		1.667	0.013
C10	p3	8	10.926	2.33	1.635	1.690			1.663	0.039
C10	p3	9	10.534	2.33	1.731	1.713	1.711		1.718	0.011
C10	p3	10	10.347	2.33	1.699	1.676	1.661		1.679	0.019
C10	p3	11	9.742	2.33	1.652	1.652	1.687		1.664	0.020
C10	p3	12	9.833	2.33	1.658	1.687	1.681		1.675	0.015
C10	p3	14	9.698	2.33	1.708	1.679	1.711		1.699	0.018
C10	p3	15	8.875	2.33	1.810	1.804	1.792		1.802	0.009
E6	p3	1	11.509	2.33	1.821	1.798	1.780	1.772	1.793	0.022
E6	p3	2	10.827	2.33	1.754	1.763	1.757	1.792	1.767	0.017
E6	p3	3	11.21	2.33	1.798	1.769	1.789	1.786	1.786	0.012
E6	p3	4	10.964	2.33	1.772	1.775	1.783	1.801	1.783	0.013

E6	p3	5	10.84	2.33	1.798	1.757	1.798	1.818	1.793	0.026
E6	p3	6	11.789	2.33	1.746	1.761	1.751	1.763	1.755	0.008
E6	p3	7	10.729	2.33	1.781	1.821	1.792		1.798	0.021
E6	p3	8	11.82	2.33	1.783	1.778	1.772	1.757	1.773	0.011
E6	p3	9	11.124	2.33	1.734	1.748	1.769	1.789	1.760	0.024
E6	p3	10	12.028	2.33	1.743	1.754	1.766	1.778	1.760	0.015
E6	p3	11	10.062	2.33	1.786	1.783	1.775	1.795	1.785	0.008
E6	p3	12	11.693	2.33	1.734	1.769	1.731	1.746	1.745	0.017
E6	p3	14	11.427	2.33	1.751	1.763	1.780	1.792	1.772	0.018
E6	p3	15	11.692	2.33	1.754	1.748	1.711		1.738	0.023
C7	p3	1	10.405	2.33	1.801	1.798	1.810	1.813	1.806	0.007
C7	p3	2	10.841	2.33	1.760	1.807	1.772		1.780	0.024
C7	p3	3	12.276	2.33	1.780	1.770	1.768	1.765	1.771	0.007
C7	p3	5	11.914	2.33	1.763	1.731	1.736	1.756	1.747	0.015
C7	p3	6	9.897	2.33	1.731	1.763	1.748		1.747	0.016
C7	p3	7	10.6	2.33	1.766	1.731	1.766	1.751	1.754	0.017
C7	p3	8	11.345	2.33	1.725	1.748	1.746		1.740	0.013
C7	p3	9	12.132	2.33	1.711	1.725	1.743	1.737	1.729	0.014
C7	p3	10	11.668	2.33	1.737	1.748	1.748		1.744	0.006
C7	p3	11	11.217	2.33	1.746	1.711	1.734	1.734	1.731	0.015
C7	p3	12	10.83	2.33	1.751	1.731	1.754		1.745	0.013
C7	p3	13	11.29	2.33	1.743	1.786	1.769		1.766	0.022
C7	p3	14	10.615	2.33	1.722	1.754	1.772	1.760	1.752	0.021
C7	p3	15	12.524	2.33	1.795	1.801	1.813	1.818	1.807	0.011
D5	p3	1	12.243	2.33	1.786	1.766	1.760	1.783	1.774	0.013
D5	p3	2	11.583	2.33	1.740	1.763	1.760	1.766	1.757	0.012
D5	p3	3	11.153	2.33	1.737	1.751	1.728		1.739	0.012
D5	p3	5	11.875	2.33	1.772	1.740	1.740	1.798	1.763	0.028
D5	p3	6	11.034	2.33	1.757	1.751	1.775		1.761	0.012
D5	p3	7	10.922	2.33	1.754	1.743	1.769	1.769	1.759	0.013
D5	p3	8	11.693	2.33	1.729	1.761	1.736	1.712	1.735	0.020
D5	p3	11	12.648	2.33	1.766	1.751	1.763	1.766	1.762	0.007
D5	p3	13	9.838	2.33	1.734	1.743	1.746	1.748	1.743	0.006
D5	p3	14	12.781	2.33	1.813	1.795	1.827	1.827	1.816	0.015
D5	p3	15	12.454	2.33	1.836	1.810	1.792		1.813	0.022
D10	p4	1	10.12	2.35	1.340	1.361	1.378	1.373	1.363	0.017
D10	p4	2	11.68	2.35	1.329	1.306	1.370	1.346	1.338	0.027
D10	p4	3	10.29	2.35	1.434	1.425	1.373	1.416	1.412	0.027
D10	p4	5	10.57	2.35	1.317	1.288	1.326		1.310	0.020
D10	p4	6	12.6	2.35	1.332	1.282	1.338	1.346	1.325	0.029
D10	p4	8	12.85	2.35	1.355	1.335	1.378		1.356	0.022
D10	p4	9	9.3	2.35	1.486	1.413	1.437	1.440	1.444	0.030

D10	p4	10	12.09	2.35	1.422	1.393	1.340		1.385	0.042
D10	p4	11	10.61	2.35	1.311	1.317	1.311	1.346	1.321	0.017
D10	p4	12	10.17	2.35	1.455	1.401	1.370		1.409	0.043
D10	p4	13	11.18	2.35	1.303	1.346	1.323	1.341	1.328	0.020
D10	p4	14	11.73	2.35	1.375	1.370	1.405	1.402	1.388	0.018
D10	p4	15	11.8	2.35	1.306	1.282	1.291	1.332	1.303	0.022
E10	p4	1	11.627	2.35	1.346	1.338	1.323	1.297	1.326	0.022
E10	p4	2	11.655	2.35	1.308	1.338	1.303	1.282	1.308	0.023
E10	p4	3	12.103	2.35	1.326	1.308	1.279	1.288	1.300	0.021
E10	p4	4	10.702	2.35	1.282	1.287	1.353		1.307	0.040
E10	p4	5	12.682	2.35	1.332	1.323	1.335	1.343	1.333	0.008
E10	p4	6	10.539	2.35	1.349	1.326	1.370		1.348	0.022
E10	p4	7	11.084	2.35	1.323	1.326	1.349		1.333	0.014
E10	p4	8	12.334	2.35	1.407	1.399	1.378	1.343	1.382	0.029
E10	p4	9	9.448	2.35	1.346	1.311	1.306	1.271	1.309	0.031
E10	p4	10	11.184	2.35	1.346	1.381	1.425	1.425	1.394	0.038
E10	p4	11	10.872	2.35	1.408	1.416	1.367	1.329	1.380	0.040
E10	p4	12	12.089	2.35	1.405	1.454	1.457	1.442	1.440	0.024
E10	p4	13	11.347	2.35	1.306	1.306	1.262	1.297	1.293	0.021
E10	p4	14	12.103	2.35	1.311	1.288	1.343		1.314	0.028
E10	p4	15	9.348	2.35	1.338	1.352	1.349		1.346	0.007
C10	p4	1	9.828	2.35	1.373	1.373	1.346	1.346	1.360	0.016
C10	p4	2	11.799	2.35	1.367	1.326	1.349	1.361	1.351	0.018
C10	p4	3	10.652	2.35	1.472	1.437	1.472	1.410	1.448	0.030
C10	p4	5	12.104	2.35	1.419	1.416	1.477	1.44	1.438	0.028
C10	p4	7	11.229	2.35	1.399	1.381	1.367	1.434	1.395	0.029
C10	p4	8	10.144	2.35	1.370	1.361	1.381	1.390	1.376	0.013
C10	p4	9	10.321	2.35	1.454	1.422	1.454		1.443	0.018
C10	p4	10	12.349	2.35	1.428	1.428	1.396	1.407	1.415	0.016
C10	p4	12	10.02	2.35	1.393	1.381	1.346		1.373	0.024
C10	p4	13	11.009	2.35	1.463	1.448	1.413	1.39	1.429	0.033
C10	p4	14	12.14	2.35	1.349	1.364	1.338	1.332	1.346	0.014
C10	p4	15	12	2.35	1.402	1.413	1.373	1.390	1.395	0.017
E6	p4	1	11.341	2.35	1.445	1.437	1.431	1.448	1.440	0.008
E6	p4	2	12.417	2.35	1.422	1.428	1.442	1.472	1.441	0.022
E6	p4	3	12.215	2.35	1.489	1.454	1.466	1.469	1.470	0.015
E6	p4	6	11.78	2.35	1.434	1.416	1.419	1.451	1.430	0.016
E6	p4	7	12.257	2.35	1.451	1.428	1.472	1.495	1.462	0.029
E6	p4	8	12.437	2.35	1.454	1.416	1.445	1.475	1.448	0.024
E6	p4	9	13.759	2.35	1.489	1.454	1.454	1.475	1.468	0.017
E6	p4	10	12.54	2.35	1.477	1.440	1.475	1.463	1.464	0.017
E6	p4	11	12.022	2.35	1.483	1.483	1.498	1.501	1.491	0.010
E6	p4	13	12.414	2.35	1.442	1.480	1.492		1.471	0.026

E6	p4	14	11.307	2.35	1.457	1.460	1.442	1.422	1.445	0.017
C7	p4	1	12.221	2.35	1.480	1.472	1.469	1.472	1.473	0.005
C7	p4	2	11.357	2.35	1.451	1.445	1.460	1.480	1.459	0.015
C7	p4	3	11.495	2.35	1.440	1.463	1.454		1.452	0.012
C7	p4	4	12	2.35	1.489	1.469	1.437	1.448	1.461	0.023
C7	p4	5	11.169	2.35	1.492	1.469	1.442		1.468	0.025
C7	p4	6	11.205	2.35	1.495	1.477	1.457		1.476	0.019
C7	p4	7	11.49	2.35	1.477	1.445	1.454	1.460	1.459	0.013
C7	p4	8	11.716	2.35	1.466	1.451	1.466	1.472	1.464	0.009
C7	p4	9	11.479	2.35	1.486	1.440	1.477		1.468	0.024
C7	p4	10	13.409	2.35	1.477	1.504	1.451	1.451	1.471	0.025
C7	p4	11	13.125	2.35	1.495	1.527	1.477	1.472	1.493	0.025
C7	p4	12	12.609	2.35	1.480	1.463	1.466	1.451	1.465	0.012
C7	p4	13	13.735	2.35	1.475	1.512	1.469	1.437	1.473	0.031
C7	p4	14	12.887	2.35	1.463	1.442	1.46	1.463	1.457	0.010
C7	p4	15	13.15	2.35	1.492	1.518	1.518	1.498	1.507	0.014
D5	p4	1	13.384	2.35	1.431	1.416	1.428	1.475	1.438	0.026
D5	p4	2	12.839	2.35	1.454	1.437	1.393	1.442	1.432	0.027
D5	p4	3	11.929	2.35	1.431	1.445	1.457	1.463	1.449	0.014
D5	p4	4	12.201	2.35	1.442	1.442	1.407	1.425	1.429	0.017
D5	p4	5	12.069	2.35	1.463	1.472	1.431	1.454	1.455	0.018
D5	p4	6	12.445	2.35	1.452	1.438	1.413	1.421	1.431	0.017
D5	p4	7	12.468	2.35	1.437	1.460	1.428	1.428	1.438	0.015
D5	p4	8	13.429	2.35	1.463	1.466	1.437		1.455	0.016
D5	p4	9	12.204	2.35	1.445	1.410	1.419	1.457	1.433	0.022
D5	p4	10	11.594	2.35	1.457	1.489	1.469		1.472	0.016
D5	p4	11	10.652	2.35	1.425	1.440	1.457		1.441	0.016
D5	p4	13	12.785	2.35	1.431	1.434	1.457	1.442	1.441	0.012
D5	p4	15	11.493	2.35	1.422	1.469	1.442	1.460	1.448	0.021

13. Appendix C: Effective in-plane elastic properties for a polycrystal with columnar grains that have one crystal axis aligned with the long axis

The relationships used to calculate the effective isotropic, in-plane elastic properties for the homogenized material in which the explicitly modeled crystals are embedded are derived here. The results are for an aggregate of cubic crystals that have: 1) one axis of material symmetry perpendicular to the surface of the material, and 2) random crystal rotations about this 3-axis. The usual contracted notation is used ($\sigma_1 = \sigma_{11}$, $\sigma_2 = \sigma_{22}$, $\sigma_3 = \sigma_{33}$, $\sigma_6 = \sigma_{12}$, $\varepsilon_1 = \varepsilon_{11}$, $\varepsilon_2 = \varepsilon_{22}$, $\varepsilon_3 = \varepsilon_{33}$, $\varepsilon_6 = 2\varepsilon_{12}$).

Cubic single crystal elastic properties are defined by 3 stiffness constants: C_{11}, C_{12}, and C_{66}. The in-plane cubic stiffness and compliance components for plane strain are

$$\begin{bmatrix} \sigma_1 \\ \sigma_2 \\ \sigma_6 \end{bmatrix} = \begin{bmatrix} C_{11}^* & C_{12}^* & 0 \\ C_{12}^* & C_{11}^* & 0 \\ 0 & 0 & C_{66}^* \end{bmatrix} \begin{bmatrix} \varepsilon_1 \\ \varepsilon_2 \\ \varepsilon_6 \end{bmatrix} \qquad \begin{aligned} C_{11}^* &= C_{11} \\ C_{12}^* &= C_{12} \\ C_{66}^* &= C_{66} \end{aligned} \qquad\text{(C1)}$$

$$\begin{bmatrix} \varepsilon_1 \\ \varepsilon_2 \\ \varepsilon_6 \end{bmatrix} = \begin{bmatrix} S_{11}^* & S_{12}^* & 0 \\ S_{12}^* & S_{11}^* & 0 \\ 0 & 0 & S_{66}^* \end{bmatrix} \begin{bmatrix} \sigma_1 \\ \sigma_2 \\ \sigma_6 \end{bmatrix} \qquad \begin{aligned} S_{11}^* &= \frac{C_{11}}{C_{11}^2 - C_{12}^2} \\ S_{12}^* &= \frac{-C_{12}}{C_{11}^2 - C_{12}^2} \\ S_{66}^* &= \frac{1}{C_{66}} \end{aligned} \qquad\text{(C2)}$$

The stiffness transformation relationships are

$$\begin{aligned} C_{11}^{*'} &= U_1 + U_3 \cos(4\theta) & U_1 &= (6C_{11}^* + 2C_{12}^* + 4C_{66}^*)/8 \\ C_{12}^{*'} &= U_4 - U_3 \cos(4\theta) & U_3 &= (2C_{11}^* - 2C_{12}^* - 4C_{66}^*)/8 \\ C_{66}^{*'} &= U_5 - U_3 \cos(4\theta) & U_4 &= (2C_{11}^* + 6C_{12}^* - 4C_{66}^*)/8 \\ C_{16}^{*'} &= -U_3 \sin(4\theta) & U_5 &= (2C_{11}^* - 2C_{12}^* + 4C_{66}^*)/8 = (U_1 - U_4)/2 \\ C_{26}^{*'} &= U_3 \sin(4\theta) & \text{note}&: U_2 = 0 \text{ when } C_{11}^* = C_{22}^* \end{aligned} \qquad\text{(C3)}$$

51

where C_{11}^*, C_{12}^*, and C_{66}^* are defined in Eq. C1. Here the 1', 2', and 3' axis are rotated about the 3 axis of the reference 1, 2, 3 cubic crystal coordinate axes, where the 3 and 3' axes are aligned. Note that θ is the angle of rotation and is measured positive for counterclockwise rotation with respect to the 1-axis. This form of the transformation relations is commonly used in composite laminate theory [19]. The transformation relationships for compliance have a similar form but must be modified since engineering shear strain (not tensor shear strain) is used

$$
\begin{array}{ll}
S_{11}^{*'} = V_1 + V_3 \cos(4\theta) & V_1 = (6S_{11}^* + 2S_{12}^* + S_{66}^*)/8 \\
S_{12}^{*'} = V_4 - V_3 \cos(4\theta) & V_3 = (2S_{11}^* - 2S_{12}^* - S_{66}^*)/8 \\
S_{66}^{*'} = V_5 - 4V_3 \cos(4\theta) & V_4 = (2S_{11}^* + 6S_{12}^* - S_{66}^*)/8 \\
S_{16}^{*'} = -2V_3 \sin(4\theta) & V_5 = (8S_{11}^* - 8S_{12}^* + 4S_{66}^*)/8 = 2(V_1 - V_4) \\
S_{26}^{*'} = 2V_3 \sin(4\theta) & \text{note}: V_2 = 0 \text{ when } S_{11}^* = S_{22}^*
\end{array}
\tag{C4}
$$

where S_{11}^*, S_{12}^*, and S_{66}^* are defined in C2.

The Voigt upper bound estimate for stiffness components of a random aggregate of cubic crystals with aligned 3-axes is determined by averaging $C_{11}^{*'}, C_{12}^{*'},$ and $C_{66}^{*'}$ over all values of θ.

$$
C_{ij}^{UB} = \frac{1}{2\pi} \int_0^{2\pi} C_{ij}^{*'}(\theta) d\theta
\tag{C5}
$$

where $C_{ij}^{*'}(\theta)$ defined by Eq. C3. Note however,

$$
\int_0^{2\pi} \cos(4\theta) d\theta = 0 \text{ and } \int_0^{2\pi} \sin(4\theta) d\theta = 0
\tag{C6}
$$

Consequently, using Eq. C3

$$
C_{11}^{UB} = U_1, \ C_{12}^{UB} = U_4, \text{and } C_{66}^{UB} = U_5 = (U_1 - U_4)/2
\tag{C7}
$$

In a completely analogous manner (using Eqs. C4), it can be shown that the Reuss upper bound limit for compliance constants (lower bound estimate for stiffness constants) for a random aggregate of cubic crystals with aligned 3-axes is

$$S_{11}^{UB} = V_1, \quad S_{12}^{UB} = V_4, \text{and} \quad S_{66}^{UB} = V_5 = 2(V_1 - V_4) \tag{C8}$$

This can be expressed in terms of a lower bound on stiffness constants

$$C_{11}^{LB} = \frac{V_1}{V_1^2 - V_4^2}$$

$$C_{12}^{LB} = \frac{-V_4}{V_1^2 - V_4^2} \tag{C9}$$

$$C_{66}^{LB} = \frac{1}{V_5} = \frac{1}{2(V_1 - V_4)}$$

The above results can be used to determine the exact value of a biaxial modulus M of a random aggregate of cubic crystals with aligned out-of-plane crystal axes. Using Eqs. C3 and C7, the upper bound for the biaxial modulus M^{UB} is given by

$$M^{UB} = C_{11}^{UB} + C_{12}^{UB} = U_1 + U_2 = C_{11}^* + C_{12}^* \tag{C10}$$

Likewise, using Eqs. C4 and C8, the lower bound for the biaxial modulus, M^{LB}, is given by

$$M^{LB} = C_{11}^{LB} + C_{12}^{LB} = \frac{1}{V_1 + V_4} = \frac{1}{S_{11}^* + S_{12}^*} \tag{C11}$$

Consequently,

$$M^{UB} = M^{LB} = M = C_{11}^* + C_{12}^* \tag{C12}$$

since $C_{11}^* + C_{12}^* = 1/(S_{11}^* + S_{12}^*)$ (Eqs. C1 and C2).

Two elastic constants are needed to define the effective isotropic, in-plane elastic properties, and one of those, M, is known exactly. A reasonable choice for the second

53

constant C_{11}^e, is defined as the average of its upper and lower bound estimates (C7 and

C9). Effective values of Young's modulus E^e and Poisson's ratio ν^e can be determined

using well-known relationships between stiffness constants and Young's modulus E and

Poisson's ratio ν, and the fact that $C_{12}^e = C_{11}^* + C_{12}^* - C_{11}^e$ (Eq. C12).

$$\nu^e = C_{12}^e / (C_{11}^e + C_{12}^e) \quad \text{and} \quad E^e = (1+\nu^e)(1-2\nu^e)C_{11}^e / (1-\nu^e)$$

Note that the effective plane stress modulii can be derived in an entirely analogous

manner by simply replacing Eqs. C1 and C2 with the appropriate plane stress stiffness

and compliance terms.

14. Appendix D: Investigation of intra and inter granular stress distribution in SUMMiT V polysilicon using electron back scatter diffraction and confocal Raman microscopy – Feasibility studies, Siddharth S. Hazra, Jack L. Beuth Jr., Maarten P. de Boer, (Carnegie Mellon University) and Ryan P. Koseski, Frank Del Rio, Mark Vaudin (NIST, Gaithersburg, Md).

This appendix describes a preliminary study on in-situ stress measurement techniques that was funded by the present LDRD and was performed at NIST, Gaithersburg, Maryland during the months of June through September, 2010. Stress concentrations (i.e., stress singularities within the context of elasticity theory) occur at flaws such as nanonotches and grain triple junctions at free surfaces as well as internal triple junctions. These locations are the presumed points where failure initiates in structures manufactured in the SUMMiT V process. In-situ high resolution stress characterization techniques that validate and directly quantify the local stresses have not been previously explored. The goal of this work is to observe the existence of such stress concentrations, and obtain direct evidence about which of these flaws constitutes the most likely fracture initiation site. The on-chip micro tensile tester that was developed as part of the current LDRD provides a unique opportunity to apply advanced experimental techniques to examine stress fields with nanoscale resolution in a tensile-loaded specimen. We evaluate the feasibility of using confocal Raman microscopy (CRM) and Electron Backscatter Diffraction (EBSD) methods for obtaining stated data.

Expertise with the Raman microscopy approach was developed from CRM studies of the stress fields around wedge indents in single crystal silicon. However, the observed shifts in the Raman shift in the optical phonon modes as a function of stress has been extensively documented for single crystal silicon. It is relatively well-known how Raman peak shifts correspond to variations in the local strain tensor relative to an assumed unstressed far-field region. Similar knowledge is relatively unavailable for polycrystalline silicon. In spite of this, since Raman shifts correspond injectively and directly to the relative local strain, obtaining the shift information is sufficient to visualize how the stress varies in structures. Besides this limitation of unknown proportionality of Raman peak shift-to-strain conversion parameters (phonon deformation potentials) the only restriction is the resolution of Raman microscopy, which is around 200 nm. Since polysilicon grains from the SUMMiT V process are known to be around that size, CRM is unlikely to yield information on inter and intra granular stress distributions in the current state of the art. However, the spectral imaging technique allows for the construction of Raman shift maps over larger areas describing the global state of stress over such area.

EBSD consists of the collection of electrons from a field emission scanning electron microscope (FE-SEM) gun backscattered from the sample of interest on a phosphor detector. If the sample is crystalline in nature, the back scattered electrons exhibit kikuchi electron backscatter diffraction patterns (EBSP) on the detector. An analysis of such diffraction patterns can reveal the state of strain or grain rotation within the crystal through comparative image analysis (cross-correlation) techniques. Though EBSD works very well for large grained or single crystal material, there are numerous issues with the

EBSP obtained from polysilicon grains discussed later. Again, the state of strain/stress determined with EBSD is a relative measurement.

Design of in situ experiment hardware
The samples to be tested in situ were wire-bonded in 48 pin cavity DIP sockets. Each microchip on the socket contains 8 nominal designs of the microtensile tester that are of interest. For both CRM and EBSD, a hardware solution was required to supply incremental voltage to the device under observation. For the purpose of switching between devices a signal switch board was constructed (Fig. 1(a)), and a small foot print card-edge socket board (Fig. 1(b)) was constructed for supplying the cavity DIP socket with signals from the switchboard.

Provisional in situ method
To vary the force applied to the tensile bar without controlling the applied voltage to the device, the number of legs on existing thermal actuators could be varied by removing a number of legs prior to engaging the device. This would allow the application of stresses lower than the fracture strength of polysilicon after the applied voltage was dropped to zero. With this approach, an experiment could be designed where the number of legs varied from 5 through 8 without the need for in situ hardware. The set of such experiments would essentially replicate the behavior of the in situ experiments with fewer load steps. Figure 2 shows an example of a provisional in situ thermal actuator. Data can only be obtained from the CRM experiments however, since it does not allow the collection of a reference DP for EBSD (more discussion follows). This approach enabled examination of techniques as well as preliminary investigations of data.
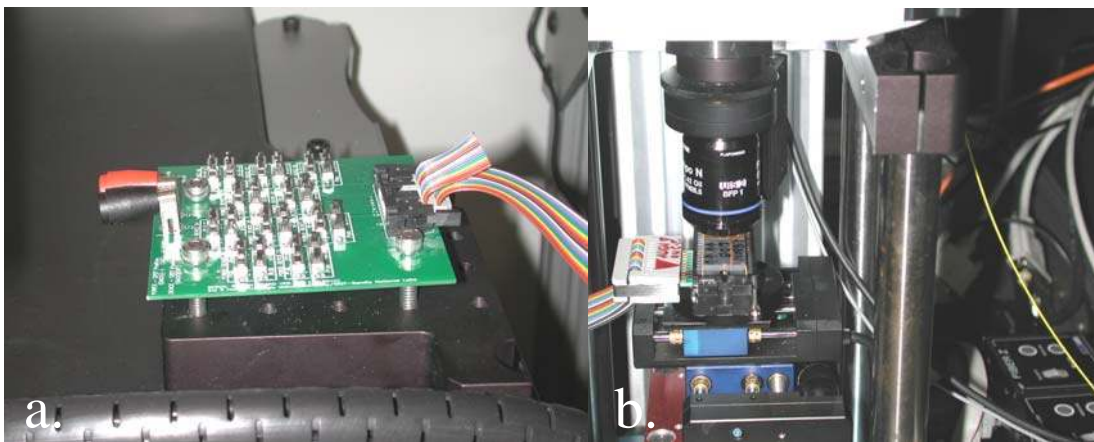

Figure 1. In situ hardware under the CRM experimental setup. (a) Signal switch board – Used to supply voltage to the selected wire-bonded device mounted on the card edge socket board in (b).
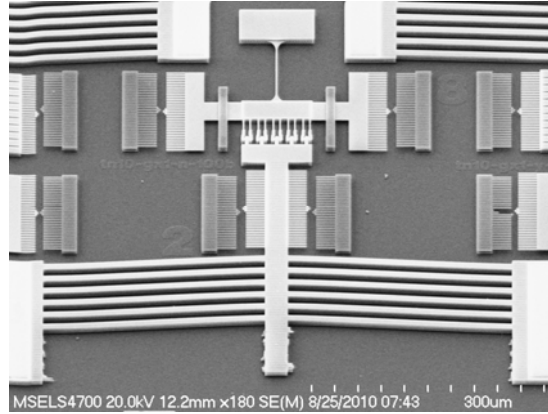
Figure 2. Provisional in situ experiment device with 6 legs.

Approach to CRM

The application of CRM to the tensile samples proved to be straightforward. Unstressed samples were placed for comparison used in the existing CRM experiment setup directly. Samples were observed in air and under optical immersion oil under diode laser (405 nm wavelength) illumination. A significant improvement in resolution was observed with the use of immersion oil. Figure 3(a) shows the Raman peak shifts observed from a provisional in situ device with 7 thermal actuator legs. The shift contours are observed to be very similar to those obtained from finite elements analysis of a loaded tensile sample shown in Fig. 3(b). As mentioned earlier, the principal hindrance to obtaining stresses from the Raman shifts are the unknown phonon deformation potentials for polysilicon, so we are restricted to comparing shift contours with stress/strain contours obtained from FEA. This also opens the opportunity for the microtensile tester to be used for estimating, and possibly determining definitively the phonon deformation potential constants due to the characterizable nature of the standard shaped tensile bar.
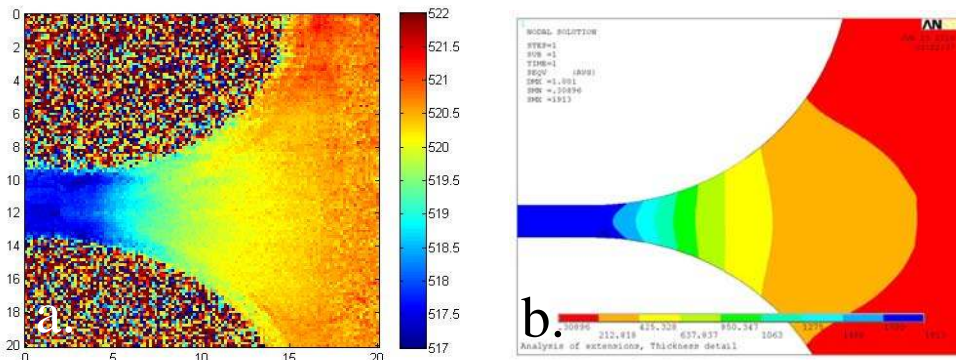
Figure 3. (a) shows the Raman peak shifts from a provisional in situ experiment on a stressed polysilicon tensile bar under oil immersion while (b) shows the stress distribution the same region from a finite elements simulation.

Initial in situ experiments using the hardware discussed above were also carried out. In these experiments we measured the Raman peak shifts over a line across the sample width as a function of applied voltage resulting in two measurements, each consisting of 4-6 data points originating from the tensile bar material. The results are shown in Fig 4. The voltage is dropped from the right to left. The higher shifts observed after sample fracture are currently being attributed to a loss in focus of the laser since the sample shifts in space after fracture. More experiments to produce reportable data are being carried out on both provisional in situ and actual in situ samples. It is also envisioned that CRM will prove to be an excellent tool in an investigation of stress fields around notched tensile samples created as a part of the current LDRD
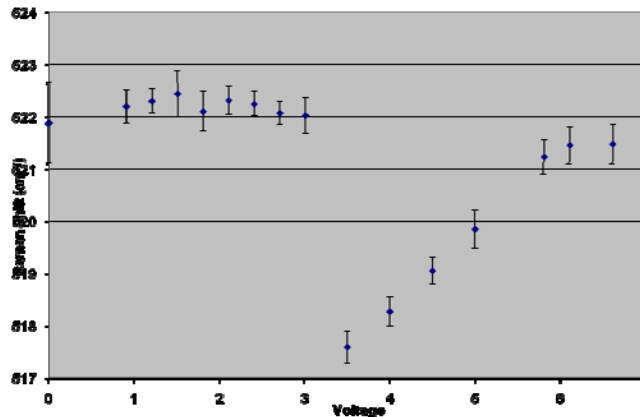
Figure 4. shows the Raman shifts in air from an in situ experiment over a line scanned across the width of the tensile sample as a function of the applied voltage.

Approach to EBSD

EBSD studies use diffraction patterns obtained from electrons backscattered from the sample. For monocrystalline material, since the orientation of the crystal lattice is uniform, strains through the sample geometry can be obtained by correlating the EBSP from an unstressed location with those from a stressed location. The standard technique is not as straight-forward for polycrystalline samples due to the inhomogeneous crystal orientations through multiple grains. The multiple grains in polysilicon, assumed to be oriented randomly, produce multiple patterns resulting in the detection of multiple overlaid patterns (shown in Fig. 5(b)). Therefore, the only possibility of determining inter and intra granular strains within polysilicon samples are when experiments are conducted in situ; this allows correlation between DP obtained from the same grains under observations as the state of stress is varied. This therefore restricts the scope of provisional in situ experiments. However, if the grains could be identified in the provisional in situ samples, then comparative intragranular stress distributions would still be identified. At the time of initiation of the project it was not clear that EBSPs originating from polysilicon samples would exhibit sufficient resolution to be processed using automated pattern detection and recognition techniques. The provisional in situ samples proved to be invaluable in optimizing the parameters determining EBSP clarity.
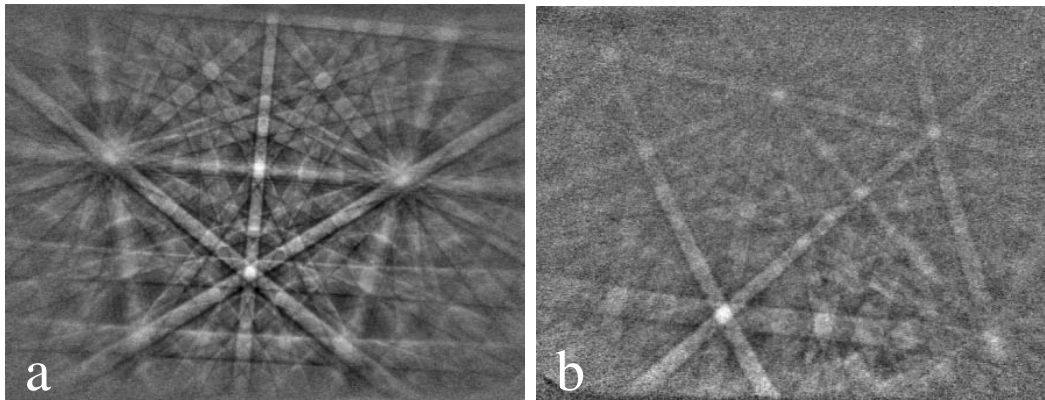
Figure 5. (a) Diffraction pattern exhibited by monocrystalline silicon. (b) Diffraction pattern observed for polycrystalline silicon. Note the distinct lack of contrast, multiple overlaid patterns, low signal to noise ratio.

EBSD primarily consists of three operation steps: obtaining a good estimate of the working distance between the sample and the electron gun, optimizing the sample stage to diffraction pattern detector geometry and optimizing the automated image processing software that identifies the phase and orientation of the sample. The first step, of estimating the sample working distance, is achieved by maximizing the clarity, focus and feature resolution of the SEM image monitor and utilizing the internal SEM software to determine the working distance. These parameters are governed by the physics of electron optics. Acceleration voltage and electron current are significant parameters. Image drift due to sample charging will alter measurements and should be reduced or eliminated by reducing the electron current. This is problematic as EBSP image quality is directly proportional to the electron current magnitude.
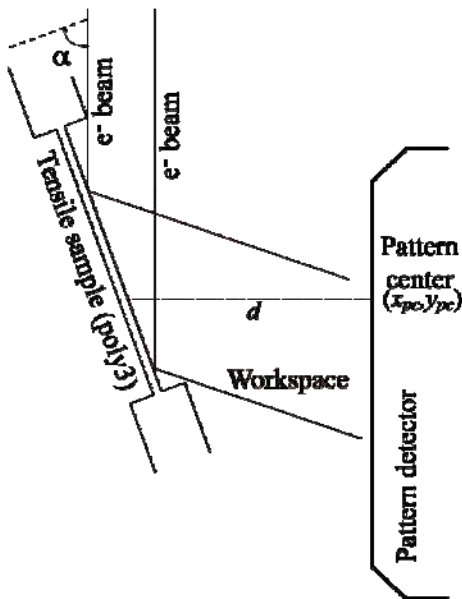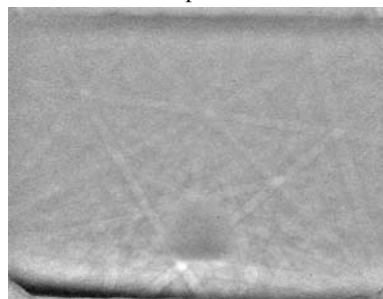

Figure 6. Shows the geometric and workspace constraints on the EBSD from the poly4 ledges on the tensile sample. Any obstruction shows across as a shadow across the screen as shown below. The location of the shadow depends upon whether the beam is focused at the top or bottom of the sample.

The second operation step, sample stage to detector geometry optimization, influences the clarity of the DP by maximizing the number of backscattered electrons to the detector. This can be done by varying the sample tilt (α), the sample elevation and detector distance (d) as shown in Fig. 6. Since the samples were not designed with EBSD sample geometry in mind, a major issue we encountered was that some of the electrons were being shielded by the poly4 structural layers at the end of devices constructed in the poly3 layer. This resulted in lower contrast as well as a shadow over the EBSP (inset of Fig. 6). Variations of the sample stage geometry were tried again to minimize the shielding. Since we had samples constructed in poly4 available on the chips used for provisional in situ experiments which would not suffer from shielding, the preliminary EBSD experiments were designed based on these samples (shown in fig. 7).
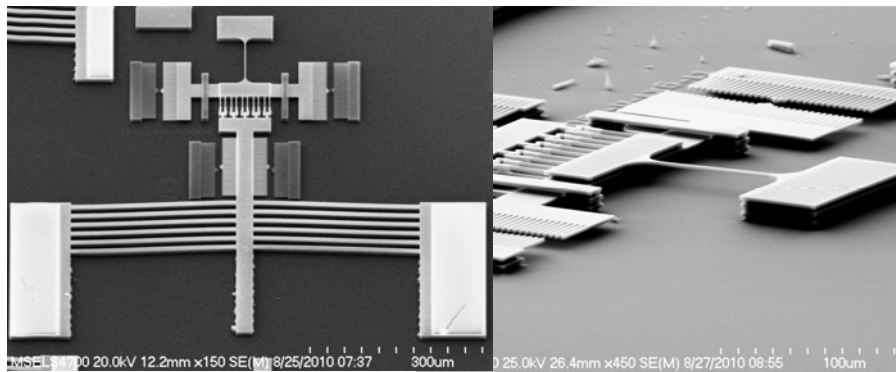

Figure 7. A poly4 provisional in situ EBSD tensile specimen with six legs. The image on the right shows the poly4 sample in perspective

The third operation step for EBSD is to automate the EBSP acquisition and identification procedure. For this purpose the Oxford instruments HKL Flamenco software was used. First the representative background is collected for subtraction from the diffraction pattern image and then the pattern is analyzed for lines using the Hough transform. The software then classifies the detected lines to obtain crystal orientation. Some of the key variables upon which this classification depends are the pattern center coordinates and the detector distance. Other variables are the number of scans and the time to collect electrons on the detector, these while not critical to the EBSD process, assume importance if the sample under observation show drift, for example.

A holistic approach to the optimization of the above mentioned parameters was taken rather than a systematic study in light of the short duration of the project. DP of resolution sufficient for pattern identification was found at 68° sample tilt in relation to the flat original stage surface (22° to the incident beam), 12 mm sample elevation, 25 kV acceleration voltage, 30 nA electron current, 21.6 mm working distance, 2×2 binning for background collection over 350 ms time intervals. To obtain accurate diffraction pattern optimization a more extensive study will be needed, but these values proved to be sufficient to generate indexed patterns in poly4 samples.

Figure 8(b) shows a grain map obtained from a poly3 tensile bar overlaid across the SEM micrograph, Fig. 7(a), of the tensile sample fillet structure. The patterns were indexed with a success rate of 78% in this case. However only a single grain is obtained of sufficient size to determine intragranular stresses, and some of the indexed regions appear to be noise and small grains (more successful cases are presented later). Significant drift can be noted in the lower section of Fig. 8(a) along with recognizable grain boundaries. A consistently observed problem is EBSPs from grain boundary regions are almost always comprised of multiple overlaid patterns.
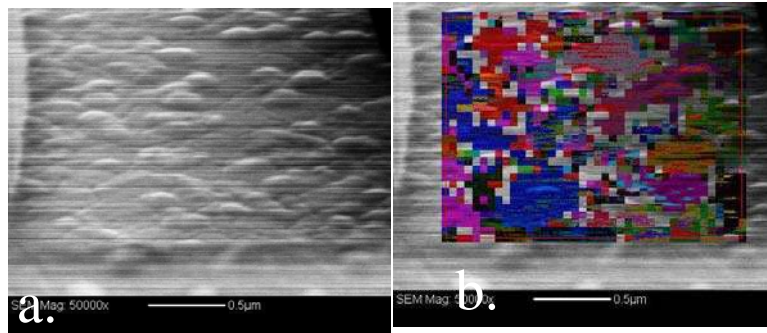
Figure 8. (a) SEM micrograph of a 70° tilted tensile sample neck region.
(b) shows the indexed grain map overlaid across (a).

Once indexed, Crosscourt diffraction pattern analysis software deduces the displacement gradient tensor, from which the strain tensor is calculated. Figure 9 shows the intragranular stresses obtained from the grain in the lower left corner of Fig 8(b) (indexed as a blue region) using this software. The distribution qualitatively follows expectations since the fillet end of the tensile bar lies south of the grain while the TB gage section is to the north.
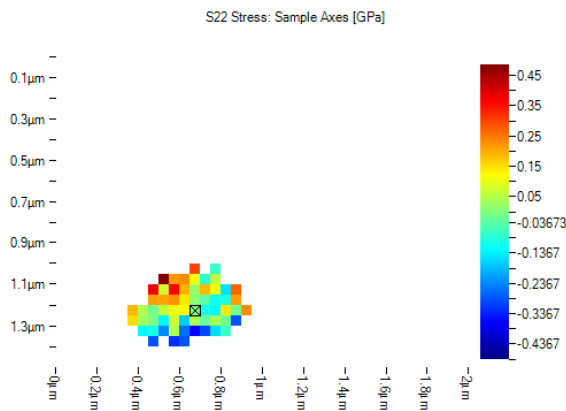

Figure 9. Intragranular stress distribution from the sufficiently large grain obtained in Fig. 9(b). The pixel marked with a crossed square represents the diffraction pattern with respect to which stresses inside the grain have been calculated. The distribution follows expectations since the fillet end of the tensile bar lies south of the grain while the TB gage section is to the north. However the magnitude of stress variation seems larger than normal for a single grain. Further investigations are required to

The following images come from studies of the poly4 tensile bar structural layer, after the rough optimization parameters were obtained. We were successful in eliminating drift of the sample to a great extent. However this was at a slight cost to the EBSP clarity and contrast. Flamenco analysis software is capable of detecting and classifying such patterns, but with noticeable reduction in overall indexing success rate (reduced to about 50-60%). However, the cost is offset by a significant increase in regions indexed as single grains and reduction in noisy identifications.

Figure 10 shows two grain maps, with (a) being a region 20×25 pixels and (b) being 30×32 pixels, with each pixel representing a step of 15 nm and 25 nm respectively. The grain map of (a) comes from a region centrally located within the gage length of the tensile sample, and that of (b) focuses on a sidewall notch. The grains in the above images have not currently been analyzed for intragranular strain.
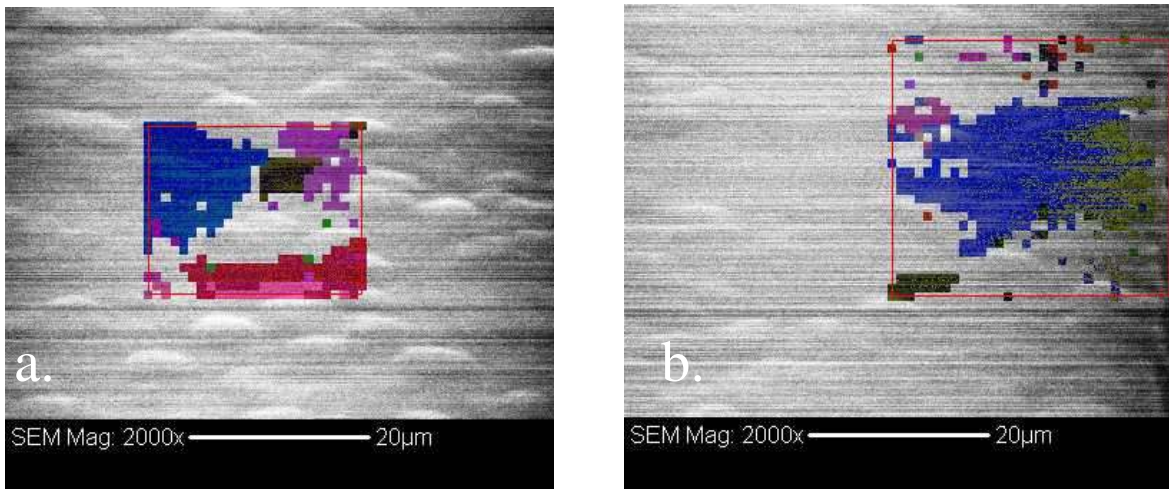

Figure 10. Grain maps obtained from analysis of a (a) large grain with noticeable boundaries in the middle of a poly4 sample gage section, at 68° tilt, and, (b) clear sidewall flaw close to the tensile bar fillet region of the same sample.

The set of above images demonstrate that it is indeed possible to extract and index the diffraction maps from polycrystalline silicon samples at a pixel size of 15 and 25 nm, respectively. However we still require carrying out an extensive optimization of all the parameters that govern both DP image acquisition and processing.

It was noted earlier that we require the in situ EBSD experimentation to map *intergranular* stress distributions, where undeformed/unstressed reference diffraction
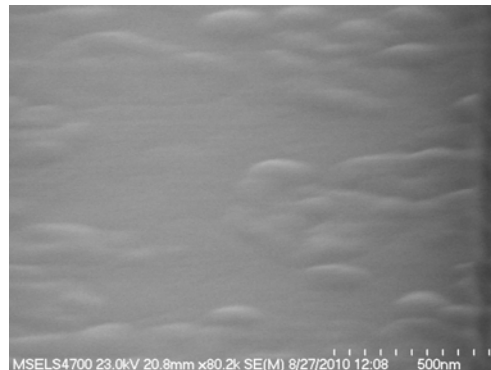

Figure 11. SEM micrograph of the background from Fig. 9(b). The sidewall notches can prove to be machine identifiable.

patterns can be obtained before initiating the experiments. However, some problems that could manifest are a loss in focus of the electron beam, as well as a mechanical, strain-induced displacement of the sample. To overcome such issues, it appears we would need to implement autofocus routines as well as image feature based autolocation. It can be seen from Fig. 11, that distinguishing features of individual grains can be manually located and selected. The feature-based autolocation routine could be based on pattern matching techniques. The principal issue would be in obtaining the high level of control over the SEM software required to implement such routines. Manual control can be implemented immediately.

Summary

In summary, we have shown CRM *in situ* and *ex situ* studies with polysilicon samples are entirely feasible, CRM will yield data for stress distributions over larger areas, which can be insightful in conjunction with EBSD. EBSD studies have shown that in-situ experimentation is a necessary precursor to polysilicon inter- and intra- granular stress distribution investigations. The feasibility of obtaining EBSP with EBSD with 15 nm resolutions for polysilicon has been demonstrated. Initially, mechanically induced displacement can be overcome by manual a alignment process. Automation of the SEM-EBSD would be useful in obtaining large datasets. The process of acquiring EBSD and granular stress distribution in stressed polysilicon samples is possible in an EBSD-capable SEM at Carnegie Mellon University. A CRM could likewise be constructed at CMU; however, environmental controls at the AML facility at NIST are a considerable factor in the demonstrated capabilities in this study.

Distribution: